npj Vaccines

https://doi.org/10.1038/s41541-026-01407-x

Article in Press

An innovative nasal nanovaccine against SARS-CoV-2 induces systemic and upper airway immunity controlling viral replication

Received: 10 July 2025

Accepted: 8 February 2026

Cite this article as: Pagni, R.L., Cunha-Neto, E., Santos, Y.d. *et al.* An innovative nasal nanovaccine against SARS-CoV-2 induces systemic and upper airway immunity controlling viral replication. *npj Vaccines* (2026). https://doi.org/10.1038/s41541-026-01407-x

Roberta L. Pagni, Edecio Cunha-Neto, Yasmin da Silva Santos, Edilberto Postól, Raquel Elaine de Alencar, Ana Moretti, Jonnatan J. Santos, Tamires L. Silva, Isabela P. Daher, Marcos C. Knirsch, João Paulo S. Nunes, Sergio H. Toma, Koiti Araki, Cesar Remuzgo, Lucas Cauê Jacintho, Lea Maria Demarchi, Vivian Leite de Oliveira, Verônica Coelho, Silvia Beatriz Boscardin, Daniela S. Rosa, João Victor Batalha-Carvalho, Ana Maria Moro, Keity S. Santos, Marco Antonio Stephano, Jorge Kalil & On behalf of COVID-19 Brazil Team

An innovative nasal nanovaccine against SARS-CoV-2 induces systemic and upper airway immunity controlling viral replication

Roberta L. Pagni[1,2,3], Edecio Cunha-Neto[1,2,3], Yasmin da Silva Santos[4], Edilberto Postól[1,2,3], Raquel Elaine de Alencar[1,2,3], Ana Moretti[1,2,3], Jonnatan J. Santos[1,2,5], Tamires L. Silva[1,2,3], Isabela P. Daher[1,2,3], Marcos C. Knirsch[6], João Paulo S. Nunes[1,2,3], Sergio H. Toma[5], Koiti Araki[5], Cesar Remuzgo[2], Lucas Cauê Jacintho[2], Lea Maria Demarchi[1], Vivian Leite de Oliveira[1,2,3], Verônica Coelho[1,2,3], Silvia Beatriz Boscardin[3,7], Daniela S. Rosa[3,8], João Victor Batalha-Carvalho[9], Ana Maria Moro[3,9], Keity S. Santos[1,2,3], Marco Antonio Stephano[6], Jorge Kalil[1,2,3]* on behalf of COVID-19 Brazil Team

1 Disciplina de Imunologia Clínica e Alergia, Departamento de Clínica Médica, Faculdade de Medicina da Universidade de São Paulo, São Paulo, Brazil. 2 Laboratório de Imunologia, LIM-19, Instituto do Coração (InCor), Hospital das Clínicas da Faculdade de Medicina da Universidade de São Paulo (HCFMUSP), São Paulo, Brazil. 3 Instituto de Investigação em Imunologia - Instituto Nacional de Ciências e Tecnologia (iii-INCT), Universidade de São Paulo, São Paulo, Brazil. 4 Departamento de Análises Clínicas e Toxicológicas, Faculdade de Ciências Farmacêuticas, Universidade de São Paulo, São Paulo, Brazil. 5 Departamento de Química Fundamental, Instituto de Química, Universidade de São Paulo, São Paulo, Brazil. 6 Departamento de Tecnologia Bioquímico Farmacêutica, Faculdade de Ciências Farmacêuticas, Universidade de São Paulo, São Paulo, Brazil. 7 Departamento de Parasitologia, Instituto de Ciências Biomédicas, Universidade de São Paulo, São Paulo, Brazil. 8 Departamento de Microbiologia, Imunologia e Parasitologia, Universidade Federal de São Paulo, São Paulo, Brazil. 9 Laboratório de Biofármacos, Instituto Butantan, São Paulo, Brazil. *Email: jkalil@usp.br

Abstract

Respiratory viral infections, such as influenza and coronavirus, are major threats to humankind. Injectable vaccines for SARS-CoV-2 protect against severe disease but fail to induce immunity in the upper airway mucosa, the virus entry site, thus not preventing infection and transmission. This highlights the urgent need for mucosal-targeted vaccination systems. While intranasal immunization holds promise, achieving local antigen delivery for mucosal immunity remains challenging. To address this, we designed an innovative nanoparticle system to deliver intranasal vaccines, using the receptor-binding domain (RBD) and multiple T-cell epitopes of SARS-CoV-2 antigens. Nonporous silica-based nanoparticles (SiNP) functionalized with a mucoadhesive cyclodextrin polymer (MaP) were selected as a delivery vehicle capable of adhering to and penetrating mucus. In a 3-dose regimen, the nanovaccine induced and sustained high systemic and neutralizing antibody levels for at least one year, with robust cellular responses, as well as IgA secretion in the oral and nasal cavities, providing strong protection against SARS-CoV-2 and substantially reducing viral loads in both upper and lower respiratory tracts. Our findings provide evidence that an intranasal vaccination platform combining two distinct nanoscale strategies might be crucial for inducing lasting and broad systemic and upper airway immunity, potentially controlling SARS-CoV-2 infection and transmission.

Keywords: SARS-CoV-2. Nasal vaccine. Nanoparticle delivery system. Adjuvanted-subunit nanovaccine. Respiratory mucosal immunity.

Introduction

Respiratory pathogens of zoonotic origin remain a major global health threat [1], with the COVID-19 pandemic exemplifying how respiratory infections can reshape society [2]. SARS-CoV-2 infects host cells via the spike receptor-binding domain (RBD) binding to the angiotensin-converting enzyme 2 (ACE2), predominantly expressed in the respiratory mucosa [3–5]. Although intramuscular vaccines effectively reduce severe disease and mortality [6], they offer only transient protection against viral replication and transmission, especially with emerging variants. Breakthrough infections often show nasopharyngeal viral loads comparable to those of unvaccinated individuals, reflecting limited mucosal protection [7]. This limitation stems from their poor induction of secretory IgA (sIgA) at mucosal surfaces, the primary site of infection [8]. Since nasal sIgA inversely correlates with viral load and disease severity [9], next-generation vaccines must induce both local and systemic immunity [10]. Intranasal vaccination offers a promising strategy to achieve this, providing needle-free delivery, better compliance, and scalability for pandemic use [11]. Current intranasal platforms using unmodified mRNA, live-attenuated viruses, or adenoviral vectors show inconsistent mucosal IgA responses [12–14], while anti-vector immunity [15,16] and safety concerns limit their applicability—highlighting the need for new, versatile mucosal vaccine systems.

In light of this, we developed a nanovaccine based on a hybrid system composed of nonporous (solid) silica mucus-penetrating nanoparticles (SiNPs) functionalized with the mucoadhesive semi-synthetic polymer 2-hydroxypropyl-β-cyclodextrin (HP-β-CD,

referred to as MaP) for intranasal delivery of SARS-CoV-2 antigens. SiNPs are widely used in biomedical formulations due to their tunable physicochemical properties, stability, and high biocompatibility [17–21]. These nanoparticles are under clinical investigation for immunotherapies and vaccine applications [20–22], and their favorable safety profile [23–26] is recognized by multiple regulatory agencies [27,28]. SiNPs are recognized for their ability to stabilize and deliver biomolecules, while promoting antigen cross-presentation confers intrinsic adjuvant potential [17,19]. Complementarily, MaP—a semi-synthetic, FDA- and EMA-approved cyclodextrin derivative widely used in nasal formulations [29,30]—enhances antigen stability and mucosal retention through hydrogen bonding with mucins [31–34], transiently modulates epithelial tight junctions to facilitate paracellular transport [34,35], and improves antigen uptake by immune cells [31,36,37]. MaP-containing formulations may prevent respiratory viral infections by blocking virus-host interactions [37]. Its safety and lack of ciliotoxicity or epithelial disruption have been extensively documented [38,39]. Thus, its multifunctionality establishes MaP as a strategic excipient for innovative intranasal nanoformulations [31]. Additionally, the vaccine cargo consists of the recombinant SARS-CoV-2 Spike RBD—key for neutralizing antibody induction [40]—combined with synthetic peptides containing sarbecovirus conserved $CD4^+$ and $CD8^+$ T-cell epitopes broadly recognized among convalescent individuals, ensuring broad HLA coverage [41]. The formulation includes the mucosal adjuvant poly(inosine:cytidine) [poly(I:C)], a Toll-like receptor 3 (TLR3) agonist that enhances both mucosal and systemic immunity [42,43]. Together, these components elicit a coordinated immune response with balanced sIgA and IgG production, hallmarks of protection against respiratory pathogens.

Mechanistically, MaP-functionalized SiNPs integrate structural and immunostimulatory features to optimize mucosal vaccine performance. Upon intranasal instillation, MaP forms a hydrated gel that prolongs residence time and promotes nanoparticle adhesion to the mucosa [31–33], enabling sustained SiNP release and epithelial penetration for efficient antigen uptake by antigen-presenting cells (APCs) in the nasal-associated lymphoid tissue (NALT) [31,44–46]. Ultrafine non-porous SiNPs (<20 nm) evade mucociliary clearance, are internalized by APCs, and activate the NLRP3 inflammasome via lysosomal destabilization, inducing IL-1β secretion and enhancing antigen presentation [47]. Their physicochemical features also favor antigen cross-presentation on MHC-I, driving $CD8^+$ T-cell priming and Th1-biased immunity [48–50]. Concurrently, HP-β-CD transiently extracts membrane cholesterol, increasing epithelial fluidity and paracellular permeability to enhance antigen transport across the mucosal barrier [34–36], while also acting as an innate immune modulator that triggers DAMP-mediated TBK1 and MyD88 signaling, promoting immune cell recruitment and local inflammation [31,51]. Together, SiNPs and HP-β-CD synergize to ensure prolonged mucosal retention, efficient antigen delivery, and potent innate immune activation, maximizing vaccine efficacy [44].

This cyclodextrin-polymer-modified silica nanoparticle platform offers distinctive advantages over existing vaccine technologies. Antigens adsorbed on the surface of non-porous SiNPs enable synchronized co-delivery of components to the same APCs [52]. The nanoscale size (<200 nm) allows passage through the nasal ciliary mesh without entrapment [53], while HP-β-CD enhances epithelial permeability and immune

cell recruitment [34–36]. Moreover, interactions between the nanovaccine and the nasal microbiome may enhance local immune readiness via TLR signaling and polymeric immunoglobulin receptor (pIgR) upregulation, promoting sIgA transcytosis into mucus [54]. This local stimulation, together with pro-inflammatory cues in the nasal mucosa, primes the mucosal environment for sIgA secretion and frontline protection [55,56]. Collectively, these mechanisms establish SiNP-MaP as a next-generation mucosal nanoplatform capable of overcoming key limitations of current vaccines against SARS-CoV-2 and other respiratory pathogens.

Results

Construction of the combined mucoadhesive and mucopenetrant SARS-CoV-2 nanovaccine system as a viable pharmaceutical product

Characterization of nanoparticles by transmission electron microscopy (TEM) revealed that silica nanoparticles (SiNPs) exhibited a uniform spherical morphology, regular in shape and monodisperse distribution (**Figure 1a**). Upon incorporation of the antigen–adjuvant complex (Ag–Adjv) and the mucoadhesive polymer (MaP), the SiNPs are surrounded by small electron-dense spheres, confirming the formation of the complete SiNP–MaP nanovaccine (**Figure 1b**). A schematic representation of the final formulation is illustrated in **Figure 1c**. Also, we determined the adsorption efficiency of each immunogenic component onto the SiNPs by chromatography (**Supplementary Figure 1a–d**), detecting the RBD (**Supplementary Figure 1b**), the eight synthetic peptides (**Supplementary Figure 1c**), and poly(I:C) (**Supplementary Figure 1d**), but not of the MaP excipient, due to the absence of UV-visible chromophores. Analysis of the supernatants from centrifuged formulations revealed distinct adsorption profiles. The chromatogram monitored at 214 nm (**Figure 1d**) showed only minimal residual peaks for peptides P1, P3, and P5. In contrast, a strong signal detected between 5 and 15 minutes, at both 214 nm (**Figure 1d**) and 263 nm (**Supplementary Figure 1e**), corresponded to unbound poly(I:C), demonstrating poor adsorption of this adjuvant, which was further confirmed by the calibration curve (**Supplementary Figure 1f**). These results confirm that the antigens were efficiently adsorbed onto SiNPs, while poly(I:C) appeared largely unbound under the tested conditions. Nonetheless, the increase in systemic IgG (**Supplementary Figure 2a**) and IgA (**Supplementary Figure 2b**) responses observed after the second intranasal dose—particularly in adjuvanted formulation—suggests that poly(I:C) was functionally incorporated into the nanovaccine, despite its high detectability by the quantification method.

The hydrodynamic size of SiNPs measured by DLS showed an average particle diameter of 21 nm (**Figure 1e**), while maintaining a low polydispersity index (0.07) (**Figure 1f**). However, after incorporation of the active vaccine components, the SiNP size slightly increased by a factor of 1.31, indicating efficient adsorption of antigen–adjuvant complexes (Ag-Adjv) onto the SiNPs, and by a factor of 1.35 when the SiNP-Ag-Adjv system was further functionalized with the polymer (SiNP-MaP), reaching a final average diameter of 37.4 nm (**Figure 1e**). The small polydispersity index of SiNP-MaP (0.13) indicated a narrow and favorable particle size distribution (PDI ≤ 0.3), as well as the formation of a single predominant particle population representative of the

nanovaccine (**Figure 1f**). The changes shown in **Figure 1g** reflect the layer-by-layer (LbL) assembly of the SiNPs and provide insight into the surface chemistry and biological behavior of the final nanovaccine. The initial SiNPs exhibited a zeta potential of –20.8 mV, consistent with negatively charged silanol (Si–OH) groups at neutral pH. As successive layers were added, the potential became slightly less negative (–15, –16.5, and –16.1 mV), indicating successful LbL assembly in which each coating partially neutralized the underlying charge. The particles remained globally anionic, confirming controlled surface modification rather than charge inversion. In addition, this modest reduction indicates that surface modification did not compromise nanoparticle stability, as corroborated by the consistent hydrodynamic size and low polydispersity index (**Figure 1e,f**). These findings indicate that the engineered SiNP-MaP nanovaccine exhibits a uniform and monodisperse structure, efficient antigen adsorption and functional adjuvant incorporation, and physicochemical characteristics suitable for nasal distribution.

The combined mucoadhesive and mucopenetrant SARS-CoV-2 nanovaccine delivery system increases the residence time of the antigen in the nasal cavity and biodistribution

Given the importance of increased nasal residence time for enhancing nasal immune responses, we evaluated the residence time of the RBD protein, both alone and within distinct nanoparticle formulations, using an IVIS spectrum in vivo imaging system (**Figure 2a**). We confirmed the antigen labeling in the formulations (**Supplementary Figure 3a**) and recorded maximum fluorescence intensity in the control (water, 2.25 x 10^7) and test formulations (1.13 to 2.62 x 10^8) (**Supplementary Figure 3b**). To delineate the fluorescence intensity emitted, we used naïve animals (n = 2/group, total n = 8). The formulations containing only RBD/Cy.5 (Ag), and this incorporated into MaP, SiNP, and SiNP-MaP, were instilled into the nostrils of animals (5 µL/nostril, n = 7/group) and analyzed immediately (T0) and at 3, 6, and 24 hours (T3, T6, and T24).

Immediately after instillation (T0), strong fluorescence was detected in the nasal region of mice receiving Ag and SiNP, whereas the MaP and SiNP–MaP groups exhibited significantly lower signal intensity (**Figure 2b**). At 3 h post-administration (T3), a marked decrease in fluorescence was observed in all groups (**Supplementary Figure 3c**); however, MaP and SiNP–MaP maintained a significantly higher fluorescence intensity than Ag alone and/or SiNP-associated (**Figure 2c**), and this difference persisted at 6 h (T6) (**Figure 2d**). After 24 h (T24), fluorescence was markedly reduced across all groups (**Supplementary Figure 3c**), yet detectable levels remained in the SiNP–MaP group (**Figure 2e**). The efficacy of nanovaccines is well known to depend critically on their in vivo distribution. To this end, we excised the major organs and evaluated the biodistribution of the formulated and unformulated vaccine antigen (**Figure 2a,f**). Despite the predominant fluorescence detected in the kidneys (K) of all animals immunized with the different formulations 3 hours after nasal instillation (**Supplementary Figure 3d–i**), fluorescent signals were also observed in the lungs (LG) of mice that received RBD/Cy.5 alone or incorporated into SiNP and SiNP-MaP (**Supplementary Figure 3e**), and in the liver (LV) and brain (B) of animals administered with RBD/Cy.5 associated with SiNP (**Supplementary Figure 3f,i**), while no fluorescence was detected in the hearts (H) or

spleens (S) of any group (**Supplementary Figure 3a,g**). However, 24 hours after instillation, fluorescence corresponding to free RBD/Cy.5 or to that incorporated into the different nanovaccine formulations was no longer detectable in any of the analyzed organs (**Figure 2f**). These findings suggest that the mucoadhesive polymer coating is essential for prolonged antigen retention in the nasal cavity and indicate efficient antigen clearance within 24 hours, with no evidence of undesired systemic accumulation.

Intranasal instillation of the innovative combination of mucus-penetrating and mucoadhesive nanomaterial presents a favorable histopathological profile, with no evidence of significant alterations

Histopathological analysis was performed on lung, spleen, liver, kidney, brain, and heart tissues collected one day after intranasal instillation of the different nanoparticulate formulations (**Figure 3a–l**). In the lungs, all immunized animals exhibited mild septal thickening consistent with local immune activation, whereas discrete pneumonitis and bronchiolar hyperplasia were observed in the MaP and SiNP groups (100%) (**Figure 3a,b**), suggesting adaptive epithelial repair. Accordingly, SiNP-MaP elicited mild and localized pulmonary reactivity (**Figure 3a,b**), reflecting the intranasal route and local immune stimulation. In the spleen, discrete germinal center hyperplasia was detected (100% in MaP and SiNP-MaP, 30% in SiNP), indicative of immunological activation without evidence of excessive systemic inflammation or splenic toxicity (**Figure 3c,d**). The liver showed mild Kupffer cell activation (70% in MaP and SiNP-MaP, 40% in SiNP) (**Figure 3e,f**), possibly related to particle phagocytosis. The kidneys exhibited mild vascular congestion across all intranasally treated groups, with no evidence of relevant renal toxicity (**Figure 3g,h**). In the brain, all immunized groups displayed discrete reactive microgliosis (70% in MaP and SiNP-MaP, 60% in SiNP) and absence of meningoencephalitis or neuronal necrosis, suggesting a transient response to intranasal administration; mild vascular congestion was also noted in MaP and SiNP groups (30% each) (**Figure 3i,j**). The heart maintained intact myocardial architecture without degeneration, with only mild vascular congestion in SiNP-MaP and MaP (30% each) (**Figure 3k,l**). Both immunized and control animals exhibited mild inflammatory infiltrates in all analyzed organs, with congestion and hemorrhage limited to the lungs and spleen. No splenic or hepatic congestion, intracytoplasmic material in the spleen, or necrosis or hemorrhage in the liver, kidneys, brain, or heart was detected (**Figure 3**). Collectively, these findings indicate that the hybrid SiNP-MaP system—combining mucoadhesive and mucus-penetrating properties—preserves the structural integrity of major organs and does not induce systemic toxicity, exhibiting only mild alterations associated with local immune responses elicited by the intranasal route.

Intranasal immunization with the combined mucoadhesive and mucopenetrant SARS-CoV-2 nanovaccine induces robust and durable systemic antibody responses

Anticipating further preclinical assessment, we evaluated the optimal intranasal immunization regimens with RBD and poly(I:C) adjuvant carried in silica-based nanoparticles functionalized with mucoadhesive polymer (SiNP-MaP vaccine) (**Supplementary Figure 4**), where an intermediate interval between doses (14 days)

was capable of robustly inducing high-specificity serum antibody responses (**Supplementary Figure 4a**) and a high capacity to generate neutralizing antibodies starting from the 2nd immunization (**Supplementary Figure 4b**). Additionally, we also assessed the range of concentrations of the recombinant RBD antigen to be carried by the SiNP-MaP vaccine, for which systemic humoral IgG and IgA responses (**Supplementary Figure 5a,b**) and mucosal IgA (**Supplementary Figure 5c-e**) were optimal, establishing 20 µg RBD antigen/animal as the optimal dose. We then observed the effect of the addition of synthetic peptides encoding $CD4^+$ and $CD8^+$ T-cell epitopes to the SiNP-MaP vaccine on the immunogenicity readouts. The addition of synthetic peptides to the SiNP-MaP vaccine significantly increased the anti-RBD and anti-peptide cellular immune responses starting at the 2nd immunization and boosted at the 3rd immunization (**Supplementary Figure 6a,b**), with no enhancing effect on serum neutralizing antibody and binding IgG and IgA anti-RBD antibodies (**Supplementary Figure 6c-e**) or mucosal IgA anti-RBD responses (**Supplementary Figure 6f-h**). From this point on, we added the conjugated CD4+ and CD8+ peptides to all the vaccines in all subsequent experiments. To evaluate the systemic humoral immunity elicited by candidate nanoparticulate formulations, C57BL/6 mice (n = 6 to 8/group) were immunized two weeks apart with a 3-dose regimen of the vaccine, with antigen and adjuvant either 1) carried in mucus-penetrating silica nanoparticles (SiNP vaccine), 2) functionalized with a mucoadhesive polymer (MaP vaccine), or 3) carried in silica-based nanoparticle system functionalized with a mucoadhesive polymer (SiNP-MaP vaccine) by intranasal instillation (D0, D14 and D28), and 4) for comparison purposes, a group of mice was immunized by intranasal instillation with the free active vaccine components, antigens and adjuvant (without nanoparticles, Ag-Adjv). Immunogenicity was assessed one day before the second and third immunizations (D13 and D27) and two weeks (D42), as well as six months and one year (D200 and D400) after the third immunization (**Figure 4a**). The IgG1, IgG2b, IgG2c, and IgA antibody responses were measured by ELISA, and the titers of serum neutralizing antibodies were measured using a pseudovirus assay.

The SiNP-MaP vaccine elicited anti-RBD IgG responses starting after the prime immunization, with an increase starting from the 2nd immunization, which was robustly increased after the 3rd immunization (**Figure 4b**). These anti-RBD IgG levels were maintained for at least one year after the 3rd intranasal dose (**Figure 4c**). The SiNP vaccine was able to induce detectable levels of anti-RBD serum IgG only after the 3rd immunization, while the Ag-Adjv and MaP vaccine groups failed to elicit serum anti-RBD IgG throughout the protocol (**Figure 4b**). Since serum IgG2c synthesis is directed by Th1 cytokines, while IgG1 production correlates with high levels of Th2 cytokines [57], we analyzed the profile of IgG isotypes in the sera of mice after the third immunization. As depicted in **Figures 4d** to **4f**, mice immunized with the SiNP-MaP vaccine elicited a specific IgG1 (**Figure 4d**), IgG2b (**Figure 4e**), and IgG2c (**Figure 4f**) response to RBD, significantly higher than the other groups analyzed. Our findings imply that intranasal instillation of the vaccine carried in SiNP and functionalized with MaP directed both Th1 and Th2 responses. The SiNP-MaP vaccine induced RBD-specific serum IgA antibodies starting from the 2nd intranasal immunization in some animals, with the magnitude of the response found to be superior to the other groups analyzed (**Figure 4g**); this response lasted less than 6 months after the 3rd immunization (**Figure 4h**). On the other hand, the

SiNP vaccine induced low titers of serum IgA, where few animals seroconverted after the 3rd immunization, and the Ag-Adjv and MaP vaccine groups failed to induce detectable levels of anti-RBD IgA at the evaluated times (**Figure 4g**). In addition to specific RBD binding titers, serum neutralizing antibody responses were also evaluated (**Figures 4i,j**). The SiNP-MaP vaccine induced neutralizing antibody responses against the Wuhan ancestral strain pseudovirus starting from the 2nd intranasal dose, significantly superior to the other formulations tested, and such responses were further increased after the 3rd immunization (**Figure 4i**), with neutralizing antibody detection lasting for at least 1 year after the 3rd immunization (**Figure 4j**). The Ag-Adjv and MaP vaccine groups failed to induce detectable neutralizing antibody levels (**Figure 4i**). The data shown above indicate that intranasal sensitization with a nanovaccine combining muco-penetrating and mucoadhesive strategies is associated with short-lived serum IgA responses and the induction of superior and long-lasting serum IgG and neutralizing antibody responses compared to the other vaccines.

The combined mucoadhesive and mucopenetrant intranasal SARS-CoV-2 nanovaccine induces IgA mucosal antibody responses in the upper respiratory tract

To assess the RBD-specific IgA and IgG humoral responses in the respiratory mucosa, oral (saliva), nasal (nasal lavage, NAS), and pulmonary (bronchoalveolar lavage, BALF) fluids from C57BL/6 mice (n = 8/group) intranasally immunized with a 3-dose regimen with 14-day intervals between each dose were collected two weeks after both the 2nd and 3rd intranasal immunizations and analyzed by ELISA (**Figure 5a**). The SiNP-MaP combination vaccine elicited anti-RBD binding IgA antibody titers in saliva (**Figure 5b**) and nasal lavage fluid (**Figure 5d**) starting from the second intranasal immunization, which were increased after the 3rd immunization; such mucosal fluid IgA antibodies were undetectable in the Ag-Adjv, MaP vaccine, and SiNP vaccine groups. However, IgA anti-RBD binding antibodies in BALF were poorly induced after the 3rd immunization with the SiNP-MaP combination vaccine. Such antibodies were undetectable in the other groups analyzed (**Figure 5f**). Interestingly, while RBD-specific IgG antibodies after the 3rd intranasal immunization were not detectable in the saliva of the evaluated groups (**Figure 5c**), immunization with intranasal nanoparticulate formulations SiNP or SiNP-MaP, but not MaP, induced IgG titers in the NAS (**Figure 5e**) and BALF (**Figure 5g**), where the combined SiNP-MaP strategy was significantly superior to the other groups tested. In addition, NAS and BALF neutralizing antibody responses were evaluated (**Figure 5h**). The SiNP-MaP vaccine induced neutralizing antibody responses against the Wuhan ancestral strain pseudovirus starting from the 2nd intranasal dose in NAS and after the 3rd intranasal dose in BALF samples, significantly superior to the other formulations tested, and such responses were increased with the 3rd intranasal dose (**Figure 5h**). These data indicate that intranasal sensitization with a nanovaccine combining muco-penetrating and mucoadhesive strategies induced an upper airway mucosal IgA response and a lower airway mucosal IgG response, as well as a neutralizing antibody response against the Wuhan ancestral strain pseudovirus in both airway compartments.

Intranasal instillation of the innovative combination of mucus-penetrating and

mucoadhesive nanomaterials containing the Wuhan RBD antigen reduces neutralization of the Omicron XBB.1.5 variant

The functionality of the antibodies was evaluated using pseudovirus neutralization assays against the ancestral SARS-CoV-2 Wuhan strain and the Omicron XBB.1.5 variant after two (**Figure 6a,c,e**) and three (**Figure 6b,d,f**) rounds of intranasal immunization. Serum (**Figure 6a,b**), NAS (**Figure 6c,d**), and BALF (**Figure 6e,f**) samples were collected from animals (n = 8) immunized with the SiNP-MaP vaccine on days 27 and 42 (**Figure 4a,5a**). Animals immunized with the SiNP-MaP vaccine exhibited lower neutralization titers against the Omicron XBB.1.5 variant compared with the corresponding IC50 values for the Wuhan strain after the second and third doses in serum (**Figure 6a,b**) and in NAS (**Figure 6c,d**), and after the third dose in BALF (**Figure 6e,f**). However, it can be observed that while serum neutralizing antibody titers after the third nasal instillation are 2.34 log10 lower for XBB1.5 than for the Wuhan strain (**Figure 6b**), nasal neutralizing antibodies are on average less than one log10 (0.675) lower for XBB1.5 compared to Wuhan (**Figure 6d**). These data indicate that although intranasal instillation with the nanovaccine combining mucus-penetrating and mucoadhesive strategies containing the ancestral Wuhan RBD antigen efficiently neutralized upper and lower airways as well as the systemic compartment, it showed a significantly reduced neutralization capacity against Omicron XBB.1.5.

The combined mucoadhesive and mucopenetrant nasal SARS-CoV-2 nanovaccine induces a systemic cell-mediated immune response

To assess whether nasal mucosa vaccination could elicit a systemic cellular immune response after two and three rounds of intranasal immunization, spleens were collected from animals (n = 8/group) immunized with the nanoformulations under study on days 27 and 42 (**Figure 5a**). Splenocytes were isolated and stimulated with RBD protein (**Figure 7a,b**) and a pool of peptides encoding SARS-CoV-2 $CD4^+$ and $CD8^+$ T-cell epitopes (**Figure 7c,d**) to assess whether local instillation at the mucosal site could activate a cell-mediated immune response. Antigen-specific IFN-γ-secreting cells were quantified using the ELISpot assay, with representative ELISpot wells shown in **Figure 7a,c** and quantified IFN-γ ELISpot results in **Figure 7b,d**. All animals immunized intranasally with the SiNP-MaP vaccine developed detectable splenic antigen-specific IFN-γ-secreting cells after stimulation with RBD protein (**Figure 7a,b**) or a pool of synthetic peptides containing conjugated CD4+ and CD8+ T cell epitopes (**Figure 7c,d**) since the 2nd immunization; the magnitude of response was greatly expanded after the 3rd immunization. This response was superior to the other groups analyzed; SiNP vaccine-immunized mice showed a low response to RBD stimulus after the 3rd immunization, while Adj-Adv and MaP vaccines failed to induce IFN-γ-secreting cells to any stimulus. Importantly, the presence of peptides encoding T cell epitopes of SARS-CoV-2 in the SiNP-MaP vaccine formulation was crucial for achieving amplification of cellular responses to RBD protein, which was 14-fold higher than immunization without the conjugated CD4+ and CD8+ peptides (**Supplementary Figure 6b**). In contrast, animals immunized with the SiNP vaccine developed a low number of splenic IFN-γ-secreting cells, detected in only a few animals after stimulation with RBD after the 3rd intranasal immunization, but superior to the Ag-Adjv and MaP vaccine groups (**Figure**

7a). The data above indicate that the SiNP-MaP strategy based on the combination of mucoadhesive and mucus-penetrating nanosystems is able to present T-cell epitopes from both RBD protein and synthetic peptides, activating a strong cell-mediated immune response mediated by IFN-γ-secreting cells starting from the 2nd intranasal immunization.

The combined mucoadhesive, mucopenetrant intranasal nanovaccine induces upper airway and pulmonary protection against SARS-CoV-2 challenge in K18-hACE2 humanized mice while substantially reducing viral loads

Since intranasal immunization with the SiNP-MaP vaccine against COVID-19 elicited robust local and systemic immune responses, we subsequently assessed whether immunization with the SiNP-MaP vaccine provided protection against infectious challenge with the ancestral Wuhan strain of SARS-CoV-2 in a highly susceptible K18-hACE2 mouse model [58] (**Figure 8**). The animals (n = 8/group) were immunized with the SiNP-MaP vaccine intranasally in a 3-dose regimen (every two weeks), and as controls, naïve (non-immunized and non-infected, n = 8) and placebo (immunized with SiNP-MaP without antigens and infected, n = 8) groups were used (**Figure 8a**). K18-hACE2 mice were intranasally infected 2 weeks after the 3rd immunization and monitored for 7 days post-infection (dpi). Oropharyngeal swabs were collected at 3, 5, and 7 dpi, and lungs were collected at the time of euthanasia (**Figure 8a**). Placebo-treated animals succumbed rapidly to SARS-CoV-2 infection, exhibiting significant body weight loss as early as the 1st dpi (**Figure 8b and Supplementary Figure 7a**), reaching 19% weight loss on the 6th dpi (**Figure 8b**). This group consistently displayed greater weight reduction than all other groups at every time point (**Supplementary Figure 7b–f**). Furthermore, clinical symptoms started by the 2nd dpi and were markedly more severe than in the other groups throughout the observation period (**Supplementary Figure 7h–l**), reaching maximum clinical scores on the 6th dpi (**Figure 8c**), at which all animals in the placebo group died (**Figure 8d**). In contrast, mice immunized with the SiNP–MaP vaccine exhibited minimal body weight loss, limited to 1% at the 7th dpi (**Figure 8b**), with significant differences compared with the naïve group from the 6th dpi onward (**Supplementary Figure 7f,g**). Vaccinated animals developed mild clinical symptoms from the 4th to the 6th dpi, with full recovery by the 7th dpi (**Figure 8c and Supplementary Figure 7h–l**), and were protected from mortality (**Figure 8d**).

Viral load in oropharyngeal swabs of K18-hACE2 mice intranasally immunized with the SiNP-MaP vaccine was 20-fold lower than that in the placebo group at both 3 and 5 dpi. Significantly, oropharyngeal viral loads were below detection levels in 3 and 4 immunized mice at the analyzed time points, respectively (**Figure 8e**). Viral loads in the lungs of SiNP-MaP-immunized mice were approximately 100-fold lower than in the placebo group; significantly, the viral load was undetectable in 5 animals immunized with the intranasal nanoparticle vaccine (**Figure 8f**). Pulmonary histopathology was analyzed at 4 to 7 dpi and classified according to the frequency of histopathological changes (**Figure 8g,h**). As expected, pulmonary lesions in placebo mice were severe and determined the cause of death. Immunization with the SiNP-MaP vaccine induced protection against pneumonia, vasculitis, and bronchiolitis caused by infection with the ancestral Wuhan strain of SARS-CoV-2, with minimal focal histopathological changes

(**Figure 8g**). Edema and alveolar damage were the most frequent findings in the placebo group (100%), followed by vasculitis and pneumonia (60%) and bronchiolitis (50%) (**Figure 8h**). Corroborating with our findings regarding the viral load detected in the lungs of some animals immunized with the SiNP-MaP vaccine (**Figure 8f**), edema and alveolar damage were present in 20% of these lung biopsies (**Figure 8h**). This could be attributed to tissue damage generated at the time of collection; however, it occurred at a lower frequency than in the placebo group. We observed that within the SiNP-MaP vaccinated group, lung edema and alveolar damage were only noticed in animals who had detectable lung SARS-CoV-2 RNA (**Figure 8i**). The above data indicate that intranasal immunization with the SiNP-MaP nanovaccine drastically lowered, and in some animals abolished—SARS-CoV-2 RNA at the oropharyngeal and pulmonary sites while providing protection against pneumonia, bronchiolitis, and vasculitis.

Discussion

In this study, we demonstrate that the combination of mucus-penetrating and mucoadhesive nanostructures within a hybrid intranasal platform successfully overcomes mucosal barriers, enhancing antigen immunogenicity in a murine model. The SiNP-MaP system elicited mucosal immune responses in the upper respiratory tract as well as durable systemic immunity against SARS-CoV-2, resulting in substantial protection upon viral challenge by limiting viral load at both the entry site and in the lungs. By integrating silica nanoparticles (SiNP) with the mucoadhesive polymer HP-β-CD (MaP), we developed a vaccine delivery system (SiNP-MaP) capable of prolonging antigen retention in the nasal cavity, improving mucosal uptake, and inducing long-lasting neutralizing antibody and cellular responses.

The rational design of the SiNP-MaP nanovaccine integrates physicochemical parameters that collectively explain its subsequent biological performance. The system displayed a narrow size distribution (~37 nm, PDI 0.13) and a moderately negative surface charge (–16 mV), features that ensure colloidal stability and efficient transport across the nasal mucosa, preventing rapid clearance or aggregation [59]. This slightly negative charge range (–10 to –25 mV) reflects an optimal balance between mucoadhesion and mucopenetration, promoting antigen retention and efficient access to inductive immune sites such as the NALT [60,61]. It is worth noting that although SiNP-Ag exhibited higher polydispersity, likely due to electrostatic interactions between the negatively charged SiNP surface and oppositely charged residues on the antigens, the addition of the anionic adjuvant poly(I:C) stabilized the formulation. Despite its low adsorption efficiency, poly(I:C) maintained its biological activity, suggesting that perimucosal interaction—rather than complete adsorption—is sufficient to trigger innate activation and enhance antigen uptake. Altogether, these characteristics ensure structural stability, antigen accessibility, and adjuvant functionality, supporting its translational viability as an intranasal vaccine platform.

The dual mucoadhesive–mucus-penetrating architecture of the SiNP-MaP nanovaccine increased antigen availability within the nasal cavity, ensuring sustained contact with the mucosal epithelium and the NALT [44,59,61,62]. Although MaP promoted local antigen retention, we speculate that its inability to traverse the

mucociliary layer and reach the underlying epithelium limited effective immune activation, as reflected in our findings. Similarly, although SiNPs exhibit high stability and adsorption capacity [59], these particles elicited weak or absent mucosal and systemic immune responses, underscoring that both mucoadhesion and mucopenetration are essential for optimal antigen delivery. In contrast, SiNP-MaP effectively combined intimate mucus contact with penetration into mucosal surfaces, promoting prolonged antigen availability and enhanced local uptake. In the SiNP-MaP system, excipients such as cyclodextrins likely contributed to initial retention [33,35,63], whereas the physicochemical features of the nanoparticles, spherical shape, and size (~30–40 nm) facilitated diffusion through mucus and controlled biodistribution [48,64].

After intranasal administration, both the isolated and combined nanoformulations were cleared via the mucociliary pathway and excreted within 24 hours, indicating efficient renal clearance and consistency with previous reports [65,66]. The transient pulmonary accumulation observed in SiNP and SiNP-MaP 3 hours after instillation reflects short-term retention in the highly vascularized and permeable lungs, followed by complete elimination within 24 hours through cellular degradation, lymphatic drainage, or phagocytosis by resident immune cells [67]. The minimal and temporary brain accumulation detected only for SiNP, with no persistence after 24 hours, indicates minimal translocation, consistent with the behavior of biodegradable nanoparticles with low surface charge and ~30 nm diameter, such as SiNP-MaP, which tend to remain localized and present a low risk of retrograde transport [68–70]. This contrasts with the risks of reversion, reactogenicity, and neuroinvasion through the olfactory pathways associated with live attenuated intranasal vaccines, factors that limited the use of FluMist [71] and led to the withdrawal of vaccines such as NasalFlu, associated with Bell's palsy [72]. The reversible hepatic presence and the absence of signal in the heart and spleen further support a restricted systemic biodistribution. Histopathology corroborated this safety profile, showing only mild local pulmonary alterations, along with discrete splenic hyperplasia indicative of immunological activation, and no degenerative lesions or toxicity in vital organs. This behavior differs from lipid-based or viral platforms, which may induce systemic dissemination or local inflammation [13,73], as well as polymeric or liposomal systems that may induce dose-dependent local toxicity, epithelial disruption, or chronic inflammation [63,74]. Altogether, SiNP-MaP instillation resulted in predominantly localized and transient biodistribution with minimal systemic and neural exposure, reinforcing its safety and the viability of the nanoplatform for intranasal immunization.

The physicochemical properties of the SiNP-MaP platform contribute to the efficient uptake of antigens by dendritic cells and M cells in the airways, promoting localized immune activation in the NALT [61,62], as well as intracellular antigen processing that ultimately leads to cellular activation and the induction of systemic and mucosal humoral responses [75]. In accordance with this mechanism, RBD-specific IgA was detected in nasal and salivary secretions after three doses, confirming NALT activation and validating the capacity of the intranasal route to induce localized mucosal immunity. The low levels of IgA detected in bronchoalveolar lavage fluid (BALF) likely reflect the small inoculation volume (5 µL per nostril) [76] and the mucoadhesive and mucus-penetrating nature of SiNP-MaP, which favors antigen retention and capture by local APCs rather

than deep lung deposition [59,77]. Nevertheless, the marked reduction in pulmonary viral load observed with SiNP-MaP suggests that naso/oropharyngeal IgA, with broad neutralizing activity, is sufficient to limit viral dissemination into the lower airways. This is consistent with the well-established ability of secretory IgA, even at low absolute levels, to block viral adhesion, invasion, and replication directly at epithelial surfaces [56,78]. In contrast, the anti-RBD IgG detected in BALF appears to be a plasma transudate [79], consistent with previous observations that circulating antibodies can reach the lower respiratory epithelium but not the olfactory compartment [80] and, in agreement with our findings, also do not reach the salivary environment. Thus, SiNP-MaP conferred robust protection against lethal challenge, likely reflecting enhanced NALT priming and secondary dissemination of mucosal effector cells to the lungs.

Systemically, SiNP-MaP induced robust and long-lasting IgG and IgA responses, as well as balanced IgG1/IgG2 profiles indicative of a mixed Th1/Th2 polarization [57], in addition to long-lasting neutralizing antibodies maintained for at least 12 months after the third dose. Concomitantly, an amplification of RBD- and peptide-specific IFN-γ responses was observed. Although the neutralizing activity against the Omicron XBB.1.5 variant induced by SiNP-MaP was reduced, which is consistent with the immune evasion of this lineage [81], the partial preservation of cross-neutralization suggests the recognition of conserved epitopes and reinforces the adaptability of the SiNP-MaP platform for future antigenic updates, an essential feature for next-generation intranasal vaccines against COVID-19. Notably, cross-neutralization of the XBB.1.5 variant was more pronounced in nasal fluids than in serum, in line with previous reports showing that sIgA in mucosal secretions exhibits superior variant cross-binding capacity compared with serum IgG neutralizing antibodies [82].

Among the limitations of this study, we acknowledge that only pseudovirus-based neutralization was performed, although the strong concordance with live-virus assays is well documented [83]. The IFN-γ ELISpot assay does not analyze specific T-cell subsets, such as tissue-resident memory T-cell (TRM) populations in the nasal mucosa and lungs, which justifies future investigations. Only female mice were used in the study, which typically exhibit stronger immune responses in mucosal vaccination models, but sex-based differences, which may influence the outcomes [84], should be addressed in subsequent studies. In addition, although poly(I:C) is not clinically approved [85], it was employed here as a well-established mucosal adjuvant for proof-of-concept studies, given its safety at low doses [86] and its proven ability to induce complementary immune responses in intranasal subunit vaccines [42,43]. Future work will evaluate alternative adjuvants, such as CpG, and will examine the potential of intranasal SiNP-MaP to block viral transmission. Preliminary evidence from our group indicates that two intranasal booster doses administered after primary immunization with the BNT162b2 mRNA vaccine (Pfizer-BioNTech) generate levels of mucosal and systemic immunity comparable to three intranasal doses. Antigens from current SARS-CoV-2 variants, as well as other respiratory pathogens, are being evaluated to explore the modularity of the nanoplatform.

Despite these limitations, SiNP-MaP demonstrated high immunogenicity and suitability for nasal administration. The nasal route already has regulatory precedents

(e.g., FluMist, Nasovac), including nanoparticle-based vaccines with well-defined safety profiles [87]. The next translational steps will follow the World Health Organization (WHO) guidelines for intranasal vaccine development [88], encompassing studies on local toxicity, biodistribution, and stability. Human dose extrapolation will consider body surface area normalization [89], processes will be aligned with Good Manufacturing Practices (GMP) [90], and formulation parameters will be optimized for human nasal anatomy. The availability of a lyophilized, cold-chain-independent product further supports global implementation. In conclusion, the SiNP-MaP nanoplatform represents a safe, adaptable, and highly immunogenic intranasal vaccine that directly overcomes key biological and translational limitations of current mucosal SARS-CoV-2 vaccines and provides a practical pathway for next-generation respiratory vaccines.

Methods

Non-porous silica-based nanoparticle (SiNP) synthesis

Silica nanoparticles were synthesized using the Stöber method [91]. Briefly, the synthesis was carried out in a biphasic system comprising an aqueous phase containing ammonium hydroxide as a catalyst and an organic phase composed of 100 mL of cyclohexane and 100 mL of tetraethyl orthosilicate (TEOS). One liter of the aqueous phase, at a concentration of 0.02 mol/L, was heated and maintained at 85°C in a 2 L glass reactor under constant stirring. Following temperature stabilization, the organic phase was added to the aqueous medium, generating a biphasic reaction system. The mixture was stirred continuously at a constant temperature for 12 hours. Upon completion of the reaction, the silica nanoparticle suspension was obtained by separating the organic phase from the aqueous phase, which contained the synthesized nanoparticles. The organic phase was reused in subsequent syntheses without compromising the quality of the resulting nanoparticle batches.

Antigen production

The monomeric recombinant RBD protein from the ancestral sequence (residues 319-537, pCAGGS vector, GenBank: MN908947) with a C-terminal 6x-histidine tag (SEQ ID NO: 47, with signal sequence of human IgE to ensure protein would be secreted in the medium) [92,93] was transfected into Expi293F™ cells (#A14527, Thermo Fisher) as previously described [93]. Protein purification was carried out using gravity-flow chromatography with Ni Sepharose™ 6 Fast Flow (#GE17-5318-06, Sigma-Aldrich) [94]. In addition to the recombinant RBD protein, the vaccine also includes 8 synthetic peptides, each encoding one $CD4^+$ and one $CD8^+$ T-cell epitope from SARS-CoV-2, to broaden T-cell responses (**Supplementary Table 1**). These peptides were selected from the SARS-CoV-2 proteome regions conserved among sarbecoviruses and among SARS-CoV-2 variants of concern, across 10 different SARS-CoV-2 proteins. Selected $CD4^+$ T-cell epitopes were the most promiscuous and had ample HLA class II coverage, while $CD8^+$ T-cell epitopes were selected that collectively bound to the 10 most frequent HLA class I molecules worldwide. The combination of the 8 selected $CD4^+$ and 8 selected $CD8^+$ T cell epitopes was recognized by T cells from >95% of COVID-19 convalescent subjects, as previously described [41]. The conjugated CD4+ and CD8+ peptides (31 to

35-mer) (SEQ ID NO.: 48, 51, 52, 53, and 56 to 59, which present 90% HLA coverage) contained an N-terminal lysine to increase interaction with the negatively charged silica nanoparticle, followed by one $CD4^+$ T-cell epitope, a linker sequence (GPGPG), and one $CD8^+$ T-cell epitope, and were synthesized by Watsonbio (Houston, USA) with greater than 90% purity and no amino-terminal modification.

Nanovaccine construction

The SARS-CoV-2 nanovaccine formulations were prepared via non-covalent adsorption of the active immunogenic components onto a non-porous silica nanoparticle (SiNP) matrix. To achieve this, a suspension of SiNPs (11 mg/mL) was added under stirring to a HEPES-buffered saline solution (5 mM HEPES, 15 mM NaCl) containing recombinant RBD protein (0.5 mg/mL), $CD4^+$ and $CD8^+$ conjugated peptides (25 mg/mL), and poly(I:C) (1 mg/mL; #P1530, Sigma-Aldrich), a synthetic TLR-3 agonist used as an adjuvant. These components were functionalized with a 10% (w/v) aqueous solution of the neutral hydrophilic polymer 2-hydroxypropyl-β-cyclodextrin (HP-β-CD; #332593, Sigma-Aldrich; MW ~1.38 kDa), which possesses a hydrophobic cavity. The pH of the final formulation was adjusted to 7.0 using 0.1 M NaOH.

Transmission electron microscopy

The morphology of the SiNP nanoparticles and SiNP-MaP vaccine was determined by transmission electron microscopy (TEM). Samples were prepared by adding 2 µL of a silica nanoparticle suspension (0.02 mg/mL in PBS, pH 7.4 ± 0.2) containing RBD (0.001 mg/mL), $CD4^+$ and $CD8^+$ conjugated peptides (0.05 mg/mL), poly(I:C) (0.002 mg/mL), and mucoadhesive polymer (10% w/v) onto a 400-mesh copper grid functionalized with an ultrathin carbon film (#01822-F, TED PELLA, USA). Excess liquid was removed from the grid after 10 minutes using filter paper. To improve visualization of the organic components (antigen and adjuvant), uranyl acetate was used as a contrast agent. Images were taken using the Jeol JEM-2100 equipment operating at an acceleration voltage of 200 kV.

Loading efficiency of active components

The loading efficiency of the active components—RBD (319–537), eight peptides, and the adjuvant poly(I:C)—was determined by reverse-phase high-performance liquid chromatography (RP-HPLC). After centrifugation of the formulations at 21,000 × g, the supernatant was collected and analyzed to quantify the non-incorporated fractions, and the amount adsorbed onto the silica nanoparticles was calculated by subtraction. Each component was analyzed individually. 2-hydroxypropyl-β-cyclodextrin was not quantified due to the absence of chromophoric groups detectable by UV–visible spectrophotometry. Non-adsorbed poly(I:C) was quantified using a standard curve constructed with known amounts (41.55, 83.1, and 166.2 µg), integrating the peak areas between retention times of 5–15 min. Chromatographic conditions: Waters C18 column (5 µm, 300 Å, 150 × 3.9 mm I.D.); mobile phase A: 0.1% trifluoroacetic acid (TFA) in water; mobile phase B: 60% acetonitrile (ACN) in 0.1% aqueous TFA; flow rate: 1 mL/min; gradient elution from 5% to 95% B over 30 min, followed by 100% B for 10 min.

Detection was set at 214 nm for the RBD protein and peptides and at 263 nm for poly(I:C).

Particle size, diameter, and zeta potential determination

Silica nanoparticles alone (SiNP), antigen-loaded SiNPs (SiNP-Ag), adjuvanted antigen-loaded SiNPs (SiNP-Ag-Adjv), and this system coated with the mucoadhesive polymer (SiNP-Ag-Adjv-MaP) were prepared at a concentration of 0.1 mg/mL in 0.05 mM phosphate buffer including 300 mM NaCl (pH 7.0). Dynamic light scattering (DLS) was measured on a Zetasizer Nano ZS90 (Malvern Panalytical, UK) equipped with a 4 mW He-Ne laser. All the DLS measurements were performed at 4.0°C ± 0.1°C and a scattering angle of 90°. The particle size distribution, apparent z-average hydrodynamic diameter, and polydispersity index (PDI) were calculated using the Dispersion Technology Software provided by Malvern. All readings were performed in triplicate at different time intervals. The average of three readings was reported as the actual particle size.

Virus, biosafety, and bioethics statements

The SARS-CoV-2/SP02/human/2020/BRA ancestral wild-type virus strain was kindly provided by Dr. E.L. Durigon from the Instituto de Ciências Biomédicas at Universidade de São Paulo, Brazil. The virus was cultured in vitro as previously described [95]. All experiments involving SARS-CoV-2 were conducted under protocols approved by the Institutional Animal Care and Use Committee (protocol number 8733111121) and followed standard rules approved by the laboratory biosafety guidelines required for the novel coronavirus (2019-nCoV) by the World Health Organization (WHO) [96] at the BSL3 facilities under the supervision of Dr. C. Wrenger from the Instituto de Ciências Biomédicas at Universidade de São Paulo, Brazil.

All proposed experiments involving mice in this project were conducted in accordance with the recommendations of the Federal Law 11.794 (2008), the Guide for the Care and Use of Laboratory Animals of the Brazilian National Council of Animal Experimentation (CONCEA), and the ARRIVE guidelines (https://arriveguidelines.org) and approved by the Institutional Animal Care and Use Committee (IACUC) of the Faculdade de Medicina at Universidade de São Paulo, Brazil (protocol numbers 1510/2020 and 1718/2021).

Mouse strains

SPF (specific pathogen-free) female C57BL/6 mice and K18-hACE2 transgenic mice (The Jackson Laboratory), aged six to eight weeks, obtained from the central animal facility of FMUSP, were used for vaccine immunogenicity and efficacy assays, respectively. The animals had *ad libitum* access to water and food provided with a 12-hour light/dark cycle at a temperature of 20-26°C.

Residence time of nanovaccine formulations in the nasal cavity and antigen biodistribution

C57BL/6 mice were lightly anesthetized at each reading with ketamine-xylazine

intraperitoneally and immunized with a single dose of the different vaccine formulations [RBD alone (Ag), RBD functionalized with MaP (Ag-MaP), RBD entrapped in SiNP (SiNP-Ag), and RBD carried in SiNP and functionalized with MaP (SiNP-Ag-MaP)] by nasal instillation (5 µL/nostril), where the RBD protein was labeled with Alexa Fluor 647 dye (Cy.5) (#A20006, Invitrogen). After cleaning the animals' nostrils with a paper towel, they were immediately scanned with a real-time, *in vivo* imaging system, IVIS Spectrum from PerkinElmer. Scans were performed immediately after nasal instillation (T0), as well as at 3 (T3), 6 (T6), and 24 hours (T24) post intranasal instillation, using the Cy.5 filter to detect the fluorescence of the labeled protein. Between scans, mice were returned to their cages to recover from anesthesia. Regions of interest in different organs (heart, lung, liver, spleen, kidneys, and brain) were detected and quantified at 24 hours after nasal instillation. The fluorescence intensity was quantified as the average radiant efficiency (total flux per ROI area, photons/s/cm^2) to normalize for region size.

Animal immunization

Mice were immunized intranasally with monomeric RBD (20 µg/animal/dose), conjugated CD4$^+$ and CD8$^+$ peptides (5 µg/animal/dose), and poly(I:C) (20 µg/animal/dose). These components were functionalized with the mucoadhesive polymer (MaP) or carried in a mucopenetrating nonporous silica-based nanoparticulate system (SiNP) or even entrapped in SiNP, and this system functionalized with MaP (SiNP-MaP). The simple mixture of active components (Ag-Adjv) without nanoparticulate carriers was instilled intranasally for comparison. Immunizations were performed in a volume of 5 µL/nostril for intranasal delivery, thrice at 14-day intervals. All experiments were conducted with placebo groups receiving empty SiNP-MaP (without antigens - placebo) serving as negative controls, but these were excluded from the results due to the absence of detectable immune responses, ensuring greater clarity in the data. Details of the vaccine content are provided in **Table 1**.

Table 1 - Components of the intranasal formulations

Vaccine component	Formulation					Purpose
	Placebo	Ag-Adjv	MaP vaccine	SiNP vaccine	SiNP-MaP vaccine	
RBD	✗	✓	✓	✓	✓	Recombinant antigen
Peptides	✗	✓	✓	✓	✓	Multi-epitope antigen
Poly(I:C)	✓	✓	✓	✓	✓	TLR3 adjuvant
SiNP	✓	✗	✗	✓	✓	Silica nanocarrier
MaP	✓	✗	✓	✗	✓	Polymeric excipient

Ag – antigens; Adjv – adjuvant; SiNP – silica-based nanoparticle; MaP – mucoadhesive polymer; RBD – receptor binding domain; poly(I:C) – poly(inosine:cytidine); TLR3 – Toll-like receptor 3.

Biological sample collection

At 14 days post-second and post-third dose immunization, as well as 6 months and 1 year after the third dose, blood samples were collected from the submandibular vein. Mucosal samples were collected 14 days after the second dose and after the third dose. For saliva collection, mice received 100 µL of pilocarpine hydrochloride (#P6503, Sigma-Aldrich) at 5 mg/mL (500 µg/animal) via intraperitoneal injection. To collect nasal-associated secretion (NAS) and bronchoalveolar lavage fluid (BALF) samples, the mice were anesthetized with 200 µL of ketamine (100 mg/kg, Dopalen – Ceva) and xylazine (10 mg/kg, Anasedan – Ceva) intraperitoneally, and a catheter was inserted into the mice's trachea, and 500 µL of saline solution was instilled into the bronchioles and 200 µL into the nasal cavity. Protease inhibitor (#P9599, Sigma-Aldrich) was added to the samples at 1:10 (v/v, saliva and NAS) and 1:100 (v/v, BALF). Finally, the spleen was aseptically harvested 14 days post-second and post-third dose immunization.

SARS-CoV-2 challenge

After three intranasal doses of the SiNP-MaP vaccine, K18-hACE2 transgenic mice (n = 8) were lightly sedated with isoflurane administration and intranasally challenged with 10^5 PFU (plaque-forming units) of the ancestral Wuhan live SARS-CoV-2 strain in a volume of 10 µL/nostril and observed for 7 days post-infection with daily measurements of body weight and clinical scores. The experiment was conducted with naive (non-immunized and non-infected) and placebo (immunized with SiNP-MaP without antigens and infected) groups serving as positive and negative controls, respectively. Oropharyngeal swabs were collected on days 3, 5, and 7. On day 7 post-infection (7 dpi), surviving animals were euthanized, and lungs were collected. The clinical score was assessed for behavioral changes (lethargy, difficulty breathing, hunched posture, piloerection, eye closure, and death) and recorded based on symptom severity, with scores ranging from 0 to 4, where 0 indicates the absence of clinical signs and 4 indicates severe signs. Pain signs were monitored according to the Grimace Scale for mice [97]. A humane endpoint was established using criteria such as weight loss exceeding 20%, inactivity, or unresponsiveness to external stimuli.

Measurement of SARS-CoV-2 RBD-specific antibodies

Ninety-six-well high-binding plates (#44-2404-21, Thermo Scientific) were functionalized with 200 ng/50 µL/well (for serum IgG, IgG isotypes, and IgA) or 1 µg/50 µL/well (for saliva, nasal, and bronchoalveolar lavages IgA and IgG) recombinant SARS-CoV-2 RBD antigen diluted in 0.05 M carbonate-bicarbonate buffer (pH 9.6) per well and incubated at 4 °C overnight. Plates were blocked for 1 hour at 37°C with PBS containing 0.25% (w/v) gelatin and 0.05% Tween-20 (v/v) (PBS-T-G). Samples were serially diluted from 1:100 (serum IgG and IgG isotypes), 1:5 (serum IgA), or 1:2 (saliva, nasal, and bronchoalveolar lavages IgA and IgG), starting the dilution in a 2-fold series, and applied to each well for 2 hours at 37°C. IgG, IgG isotypes, and IgA antibody levels were detected using the appropriate horseradish peroxidase (HRP)-conjugated anti-mouse IgG, IgG1, IgG2b, and IgG2c (1:8000, #1030-05, #1070-05, #1090-05, and #1079-05, Southern Biotech, respectively) or anti-mouse IgA (1:4000, #1040-05, Southern Biotech) for 1 hour at 37°C. Between the aforementioned steps, the plates were washed four times with PBS containing 0.05% Tween-20 (v/v) (PBS-T). Plates were developed for 10 minutes using

o-phenylenediamine (OPD, #P8787, Sigma Aldrich), followed by the addition of 2 M H_2SO_4 to stop the reaction, and optical density (O.D.) was read at 490 nm using an ELISA plate reader for final data acquisition. Endpoint titers were defined as the maximum dilution that gave an absorbance reading above the mean of the placebo sample.

IFN-γ ELISpot assay

ELISpot assays were performed using the Mouse Interferon-γ (IFN-γ) ELISpot Pair Kit (#551881, BD Biosciences). Under aseptic conditions, pre-coated 96-well ELISpot plates with capture antibody were blocked with R-10 [RPMI 1640 (#31800-022, Gibco) supplemented with 10% fetal bovine serum (#12657-029, Gibco), 2 mM L-glutamine (#25030-081, Gibco), 1 mM sodium pyruvate (#11360-070, Gibco), 1% vol/vol essential amino acid solution (#M7145, Sigma-Aldrich), 1% vol/vol vitamin solution (#11120-052, Gibco), and 5 x 10^{-5} M 2-mercaptoethanol (#21985-023, Gibco)] for 2 hours at room temperature. A total of 3 x 10^5 cells per well from C57BL/6 mouse spleen were plated in each well and stimulated for 14 hours at 37°C with either recombinant SARS-CoV-2 Spike RBD domain protein (10 μg/mL) or pooled peptides containing SARS-CoV-2 $CD4^+$ and $CD8^+$ T-cell epitopes (10 μg/mL). R10 was used as a negative control, and PMA (50 ng/mL; #P8139, Sigma) and ionomycin (1 μg/mL; #I3909, Sigma) were used as positive controls. The spots were developed according to the manufacturer's instructions. The spots were scanned and quantified using an AID ELISpot reader (Autoimmun Diagnostika GmbH, Germany). Spot-forming units (SFUs)/10^5 cells were calculated by subtracting the negative control wells.

Neutralization assay of pseudovirus infection

The pseudovirus neutralization was demonstrated in a previous study [98]. Briefly, the wild-type and Omicron XBB.1.5 pSARS-CoV-2 S and pNL4-3 ΔEnv-NanoLuc, carrying the optimized SARS-CoV-2 S gene and a backbone of the human immunodeficiency virus type 1, were used. At 48 hours post-transfection, viral supernatant was collected and frozen at -80°C. Serially diluted serum (5-fold dilution factor, starting at 1:50), NAS (2-fold dilution factor at 1:10), and BALF (1.5-fold dilution factor at 1:4) samples were incubated with the SARS-CoV-2 pseudovirus at 37°C for 1 hour. The sample-virus mixture was then added to a pre-seeded monolayer of HT1080-hACE2 cells. After 48 hours, the infected cells were lysed with 5x Luciferase Cell Culture Lysis reagent (#E1500, Promega), and luciferase activity was measured using the Nano-Glo system (#N1110, Promega) in a luminometer (GloMax® Navigator Microplate Luminometer). The 50% inhibitory concentration (IC50) of each sample was calculated using nonlinear regression to reflect the anti-SARS-CoV-2 potency (GraphPad Prism 8.0).

SARS-CoV-2 RNA quantification in mice oropharyngeal swab samples and lung biopsies

Total RNA from oropharyngeal swabs and lung biopsies was extracted using the RNeasy Mini kit (#74106 and #74136, Qiagen, respectively) and followed by direct amplification of the SARS-CoV-2 nucleocapsid gene and *Mus musculus Gapdh* using the Direct One-

Step RT-qPCR kit (#PCR-518L, Jena BioSciences) for swabs. For lung samples, reverse transcription of total RNA was performed using random primers (#48190011, Invitrogen) and SuperScript IV reverse transcriptase (#18090010, ThermoFisher) according to the manufacturer's instructions. Both direct duplex RT-qPCR and duplex qPCR were performed in triplicate with total RNA (oropharyngeal samples) or cDNA (lung biopsies) and master mix containing TaqMan probes for *Gapdh* VIC-MGB (#Mm99999915_g1, ThermoFisher) and SARS-CoV-2_N_gene FAM-MGB (#Vi07918637, ThermoFisher). For oropharyngeal samples, the mix included direct enzyme mix and direct reaction buffer, while for lung samples, the universal TaqMan master mix (#4440040, Applied Biosystems) was used. The cycle threshold (CT) values of the SARS-CoV-2 N gene were normalized using the CT of *Gapdh* with the following formula: $2 \times 2\Delta CT$, where ΔCT = average CT of *Gapdh* minus average CT of SARS-CoV-2_N_gene [99].

Histopathological analysis

Tissues collected at necropsy were fixed in 10% neutral buffered formalin. Sections were evaluated blindly for histopathological processing. They were dehydrated in a graded alcohol bath, embedded in paraffin, sectioned (5 µm), and stained with hematoxylin and eosin (H&E) for examination under light microscopy.

Statistical analysis

Tests were performed at least in duplicate and analyzed using GraphPad Prism 8.0 software. Experimental values were transformed into log10 for a normal distribution. One-way or two-way ANOVA followed by Tukey's post-test was used for multiple group comparisons, Student's t-test was applied for comparison between two groups, and the Wilcoxon test was used for paired samples to compare repeated measurements in a single sample. The survival curve was analyzed using log-rank statistics. Data are expressed as mean or mean ± SD. Values of $p < 0.05$ were considered statistically significant. (*) $P < 0.05$, (**) $P < 0.01$, (***) $P < 0.001$, and (****) $P < 0.0001$.

Data availability statement

The datasets generated and/or analyzed during the current study are not publicly available due to our institution does not maintain open-access data repositories and primary records are stored in secure institutional laboratory archives. All key data are provided in the Source Data file, and additional datasets are available from the corresponding author on reasonable request.

Acknowledgments

The authors would like to thank Dr. Paul Bieniasz from Rockefeller University for providing the materials for carrying out the pseudovirus neutralization tests and Dr. Carsten Wrenger and Dr. Edmarcia de Souza from Institute of Biomedical Sciences, Universidade de São Paulo, for providing the BSL3 facilities. And on behalf of Ms. Jhosiene Magawa, from Instituto do Coração, Hospital das Clínicas. This work was supported by FINEP [grant number 01.20.0009.00], CNPq [grant numbers 403701/2020-1, 403520/2020-7, and 408518/2022-7], and DECEIIS/SECTICS/MS [grant number

25000.177752/2022-11].

Author contributions

RLP developed the study, conducted preclinical assays and cellular immune response experiments, analyzed the data, and wrote the manuscript. **YSS, EP, and REA** performed preclinical assays and humoral immune response experiments. **MAS, MCK, KA, JJS, CR, and SHT** produced and characterized the nanovaccine. **AM, TLS, SBB, IPD, AMM, and JVB-C** contributed to the production of proteins and pseudoviruses and performed pseudoviral neutralization assays. **JPSN** carried out viral RNA quantification. **LMD** performed histopathological analyses. **EC-N, LCJ, DSR, KSS, and VPCVC** selected and designed the peptides included in the vaccine formulation, project administration, data validation, and funding acquisition. **VO** served as project manager and contributed to funding acquisition. **JK** conceptualized the study, supervised the project, and secured funding. All authors read and approved the final manuscript.

Competing interests

The authors declare no competing financial or non-financial interests.

Author Information

COVID-19 SP-Brazil Team

1. Ana Carolina Ares, Laboratório de Imunologia, LIM-19, Instituto do Coração (InCor), Hospital das Clínicas da Faculdade de Medicina da Universidade de São Paulo (HCFMUSP), São Paulo, Brazil.
2. Andreia Cristina Kazue Kuramoto Takara, Laboratório de Imunologia, LIM-19, Instituto do Coração (InCor), Hospital das Clínicas da Faculdade de Medicina da Universidade de São Paulo (HCFMUSP), São Paulo, Brazil.
3. Jamille Ramos de Oliveira, Laboratório de Imunologia, LIM-19, Instituto do Coração (InCor), Hospital das Clínicas da Faculdade de Medicina da Universidade de São Paulo (HCFMUSP), São Paulo, Brazil.
4. Marcio Massao Yamamoto, Departamento de Parasitologia, Instituto de Ciências Biomédicas, Universidade de São Paulo, São Paulo, Brazil.
5. Maria Lucia Carnevale Marin, Laboratório de Imunologia, LIM-19, Instituto do Coração (InCor), Hospital das Clínicas da Faculdade de Medicina da Universidade de São Paulo (HCFMUSP), São Paulo, Brazil.
6. Philippe Rodrigues Benedetti, Laboratório de Imunologia, LIM-19, Instituto do Coração (InCor), Hospital das Clínicas da Faculdade de Medicina da Universidade de São Paulo (HCFMUSP), São Paulo, Brazil.
7. Rafael Ribeiro Almeida, Laboratório de Imunologia, LIM-19, Instituto do Coração (InCor), Hospital das Clínicas da Faculdade de Medicina da Universidade de São Paulo (HCFMUSP), São Paulo, Brazil.
8. Samar Freschi de Barros, Laboratório de Imunologia, LIM-19, Instituto do Coração (InCor), Hospital das Clínicas da Faculdade de Medicina da Universidade de São Paulo (HCFMUSP), São Paulo, Brazil.
9. Sandra Maria Monteiro, Laboratório de Imunologia, LIM-19, Instituto do Coração

(InCor), Hospital das Clínicas da Faculdade de Medicina da Universidade de São Paulo (HCFMUSP), São Paulo, Brazil.
10. Selma Aliotti Palacios, Laboratório de Imunologia, LIM-19, Instituto do Coração (InCor), Hospital das Clínicas da Faculdade de Medicina da Universidade de São Paulo (HCFMUSP), São Paulo, Brazil.
11. Simone Regina dos Santos, Laboratório de Imunologia, LIM-19, Instituto do Coração (InCor), Hospital das Clínicas da Faculdade de Medicina da Universidade de São Paulo (HCFMUSP), São Paulo, Brazil.
12. Washington Robert da Silva, Laboratório de Imunologia, LIM-19, Instituto do Coração (InCor), Hospital das Clínicas da Faculdade de Medicina da Universidade de São Paulo (HCFMUSP), São Paulo, Brazil.

References

1. World Health Organization. The top 10 causes of death https://www.who.int/news-room/fact-sheets/detail/the-top-10-causes-of-death (2020).

2. World Health Organization. COVID-19 vaccine tracker and landscape https://www.who.int/publications/m/item/draft-landscape-of-covid-19-candidate-vaccines (2023).

3. Shang, J. et al. Structural basis of receptor recognition by SARS-CoV-2. *Nature* **581**, 221–4; 10.1038/s41586-020-2179-y (2020).

4. Wrapp, D. et al. Cryo-EM structure of the 2019-nCoV spike in the prefusion conformation. *Science* **367**, 1260–3; 10.1126/science.abb2507 (2020).

5. Bourgonje, A.R. et al. Angiotensin-converting enzyme 2 (ACE2), SARS-CoV-2 and the pathophysiology of coronavirus disease 2019 (COVID-19). *J. Pathol.* **251**, 228–48; 10.1002/path.5471 (2020).

6. Mohammed, I. et al. The efficacy and effectiveness of the COVID-19 vaccines in reducing infection, severity, hospitalization, and mortality: a systematic review. *Hum. Vaccin. Immunother.* **18**, 2027160; 10.1080/21645515.2022.2027160 (2022).

7. Bleier, B.S., Ramanathan, M. & Lane, A.P. COVID-19 vaccines may not prevent nasal SARS-CoV-2 infection and asymptomatic transmission. *Otolaryngol. Head Neck Surg.* **164**, 305–7; 10.1177/0194599820982633 (2020).

8. Liew, F. et al. SARS-CoV-2-specific nasal IgA wanes 9 months after hospitalisation with COVID-19 and is not induced by subsequent vaccination. *EBioMedicine* **87**, 104402; 10.1016/j.ebiom.2022.104402 (2023).

9. Fröberg, J. et al. SARS-CoV-2 mucosal antibody development and persistence and their relation to viral load and COVID-19 symptoms. *Nat. Commun.* **12**, 5621; 10.1038/s41467-021-25949-x (2021).

10. Pilapitiya, D., Wheatley, A.K. & Tan, H.-X. Mucosal vaccines for SARS-CoV-2: triumph of hope over experience. *EBioMedicine* **92**, 104585; 10.1016/j.ebiom.2023.104585 (2023).

11. Kehagia, E., Papakyriakopoulou, P. & Valsami, G. Advances in intranasal vaccine delivery: A promising non-invasive route of immunization. *Vaccine* **41**, 3589–603; 10.1016/j.vaccine.2023.05.011 (2023).

12. Slomski, A. Intranasal COVID-19 vaccine disappointing in first-in-human trial. *JAMA* **328**, 2003; 10.1001/jama.2022.18485 (2022).

13. Zhu, F. et al. Safety and efficacy of the intranasal spray SARS-CoV-2 vaccine dNS1-RBD: a multicentre, randomised, double-blind, placebo-controlled, phase 3 trial. *Lancet Respir. Med.* **11**, 1075–88; 10.1016/S2213-2600(23)00349-1 (2023).

14. Sun, B. et al. An intranasally administered adenovirus-vectored SARS-CoV-2 vaccine induces robust mucosal secretory IgA. *JCI Insight* **9**, e180784; 10.1172/jci.insight.180784 (2024).

15. Ndzouboukou, J.B., Kamara, A.A., Ullah, N., Lei, Q. & Fan, X.L. A Meta-analysis on the immunogenicity of homologous versus heterologous immunization regimens against SARS-CoV-2 Beta, Delta, and Omicron BA.1 VoCs in healthy adults. *J. Microbiol. Biotechnol.* **35**, e2411059; 10.4014/jmb.2411.11059 (2025).

16. Nissilä, E., et al. The COVID-19 vaccine ChAdOx1 is opsonized by anti-vector antibodies that activate complement and promote viral vector phagocytosis. *Scand. J. Immunol.* **101**, e70000; 10.1111/sji.70000 (2025).

17. Yang, Y., Zhang, M., Song, H. & Yu, C. Silica-Based Nanoparticles for Biomedical Applications: From Nanocarriers to Biomodulators. *Acc. Chem. Res.* **53**, 1545–56; 10.1021/acs.accounts.0c00280 (2020).

18. Liljenström, C., Lazarevic, D. & Finnveden, G. Silicon-based nanomaterials in a life-cycle perspective, including a case study on self-cleaning coatings. *KTH Royal Institute of Technology* (2013).

19. Tang, L. & Cheng, J. Nonporous silica nanoparticles for nanomedicine application. *Nano Today* **8**, 290–312; 10.1016/j.nantod.2013.04.007 (2013).

20. Janjua, T.I., Cao, Y., Yu, C. & Popat, A. Clinical translation of silica nanoparticles. *Nat. Rev. Mater.* **6**, 1072–4; 10.1038/s41578-021-00385-x (2021).

21. Tan, A., Eskandar, N.G., Rao, S. & Prestidge, C.A. First in man bioavailability and tolerability studies of a silica–lipid hybrid (Lipoceramic) formulation: a Phase I study with ibuprofen. *Drug Deliv. Transl. Res.* **4**, 212–21; 10.1007/s13346-013-0172-9 (2014).

22. Meola, T.R., Abuhelwa, A.Y., Joyce, P., Clifton, P. & Prestidge, C.A. A safety, tolerability, and pharmacokinetic study of a novel simvastatin silica-lipid hybrid

formulation in healthy male participants. *Drug Deliv. Transl. Res.* **11**, 1261–72; 10.1007/s13346-020-00853-x (2021).

23. Barandeh, F. et al. Organically modified silica nanoparticles are biocompatible and can be targeted to neurons in vivo. *PLoS One* **7**, e29424; 10.1371/journal.pone.0029424 (2012).

24. Brown, S.C. et al. Influence of shape, adhesion and simulated lung mechanics on amorphous silica nanoparticle toxicity. *Advanced Powder Technology* **18**, 69–79; 10.1163/156855207779768214 (2007).

25. Fruijtier-Pölloth, C. The toxicological mode of action and the safety of synthetic amorphous silica-a nanostructured material. *Toxicology* **294**, 61–79; 10.1016/j.tox.2012.02.001 (2012).

26. Yu, T., Greish, K., McGill, L.D., Ray, A. & Ghandehari, H. Influence of geometry, porosity, and surface characteristics of silica nanoparticles on acute toxicity: their vasculature effect and tolerance threshold. *ACS Nano* **6**, 2289–301; 10.1021/nn2043803 (2012).

27. European Medicines Agency, Scientific Committee on consumer safety opinion on silica, hydrated silica, and silica surface modified with alkyl silicates (nano form) https://ec.europa.eu/health/scientific_committees/consumer_safety/docs/sccs_o_175.pdf (2015).

28. U.S Food and Drug Administration, US Food and Drug Administration GRAS Substances (SCOGS) Database—Select Committee on GRAS Substances (SCOGS) Opinion: Silicates, (n.d.) https://www.fda.gov/food/generally-recognized-safe-gras/gras-substances-scogs-database (2022).

29. FDA, 2023 U.S. FDA Drug Master Files (DMF) 1Q2023 https://www.fda.gov/media/166951/download (2023).

30. EMA, 2017 Cyclodextrins used as excipients. Report published in support of the 'Questions and answers on cyclodextrins used as excipients in medicinal products for human use' (EMA/CHMP/495747/2013) https://www.ema.europa.eu/en/documents/scientific-guideline/questions-and-answers-cyclodextrins-used-excipients-medicinal-products-human-use_en.pdf (2017).

31. Rassu, G. et al. Versatile nasal application of cyclodextrins: excipients and/or actives?. *Pharmaceutics* **13**, 1180; 10.3390/pharmaceutics13081180 (2021).

32. Marttin, E., Verhoef, J.C. & Merkus, F.W. Efficacy, safety and mechanism of cyclodextrins as absorption enhancers in nasal delivery of peptide and protein drugs. *J. Drug Target.* **6**, 17–36; 10.3109/10611869808997878 (1998).

33. Asim, M.H. et al. S-protected thiolated cyclodextrins as mucoadhesive oligomers for drug delivery. *J. Colloid Interface Sci.* **531**, 261–8; 10.1016/j.jcis.2018.07.062 (2018).

34. Jansook, P., Ogawa, N. & Loftsson, T. Cyclodextrins: structure, physicochemical properties and pharmaceutical applications. *Int. J. Pharm.* **535**, 272–84; 10.1016/j.ijpharm.2017.11.018 (2018).

35. Haimhoffer, A. et al. Cyclodextrins in drug delivery systems and their effects on biological barriers. *Sci. Pharm.* **87**, 33; 10.3390/scipharm87040033 (2019).

36. Matassoli, F.L. et al. Hydroxypropyl-beta-cyclodextrin reduces inflammatory signaling from monocytes: possible implications for suppression of HIV chronic immune activation. *mSphere* **3**, e00497–18; 10.1128/msphere.00497-18 (2018).

37. Lu, A. et al. Hydroxypropyl-beta cyclodextrin barrier prevents respiratory viral infections: a preclinical study. *Int. J. Mol. Sci.* **25**, 2061; 10.3390/ijms25042061 (2024).

38. Asai, K. et al. The effects of water-soluble cyclodextrins on the histological integrity of the rat nasal mucosa. *Int. J. Pharm.* **246**, 25–35; 10.1016/s0378-5173(02)00345-9 (2002).

39. Agu, R.U. et al. Safety assessment of selected cyclodextrin-effect of ciliary activity using a human cell suspension culture model exhibiting in-vitro ciliogenesis. *Int. J. Pharm.* **193**, 219–26; 10.1016/s0378-5173(99)00342-7 (2000).

40. Yuan, M., Liu, H., Wu, N.C. & Wilson, I.A. Recognition of the SARS-CoV-2 receptor binding domain by neutralizing antibodies. *Biochem. Biophys. Res. Commun.* **538**, 192–203; 10.1016/j.bbrc.2020.10.012 (2021).

41. Fernandes, E.R. et al. Time-dependent contraction of the SARS-CoV-2-specific T-cell responses in convalescent individuals. *JACI Global* **1**, 112–21; 10.1016/j.jacig.2022.05.002 (2022).

42. Ichinohe, T. et al. Synthetic double-stranded RNA poly(I:C) combined with mucosal vaccine protects against influenza virus infection. *J. Virol.* **79**, 2910–9; 10.1128/JVI.79.5.2910-2919.2005 (2005).

43. Sloat, B.R. & Cui, Z. Nasal immunization with anthrax protective antigen protein adjuvanted with polyriboinosinic-polyribocytidylic acid-induced strong mucosal and systemic immunities. *Pharm. Res.* **23**, 1217–26; 10.1007/s11095-006-0206-9 (2006).

44. Netsomboon, K. & Bernkop-Schnürch, A. Mucoadhesive vs. mucopenetrating particulate drug delivery. *Eur. J. Pharm. Biopharm.* **98**, 76–89; 10.1016/j.ejpb.2015.11.003 (2016).

45. Corr, S.C., Gahan, C.C.G.M. & Hill, C. M-cells: origin, morphology and role in mucosal immunity and microbial pathogenesis. *FEMS Immunol. Med. Microbiol.* **52**, 2–12, 10.1111/j.1574-695X.2007.00359.x (2008).

46. Kiyono, H. & Fukuyama, S. NALT- versus Peyer's-patch-mediated mucosal immunity. *Nat. Rev. Immunol.* **4**, 699–710; 10.1038/nri1439 (2004).

47. Gómez, D.M., Urcuqui-Inchima, S. & Hernandez, J.C. Silica nanoparticles induce NLRP3 inflammasome activation in human primary immune cells. *Innate Immun.* **23**, 697–708; 10.1177/1753425917738331 (2017).

48. Tang, L., Fan, T.M., Borst, L.B. & Cheng, J. Synthesis and biological response of size-specific, monodisperse drug-silica nanoconjugates. *ACS Nano* **6**, 3954–66; 10.1021/nn300149c (2012).

49. Hirai, T. et al. Amorphous silica nanoparticles enhance cross-presentation in murine dendritic cells. *Biochem. Biophys. Res. Commun.* **427**, 553–6; 10.1016/j.bbrc.2012.09.095 (2012).

50. Vis, B. et al. Non-functionalized ultrasmall silica nanoparticles directly and size-selectively activate T cells. *ACS Nano* **12**, 10843–54; 10.1021/acsnano.8b03363 (2018).

51. Onishi, M. et al. Hydroxypropyl-beta-cyclodextrin spikes local inflammation that induces Th2 cell and T follicular helper cell responses to the coadministered antigen. *J. Immunol.* (Baltimore, Md: 1950) **194**, 2673–82; 10.4049/jimmunol.1402027 (2015).

52. Sanità, G., Carrese, B. & Lamberti, A. Nanoparticle surface functionalization: how to improve biocompatibility and cellular internalization. *Front. Mol. Biosci.* **7**, 587012; 10.3389/fmolb.2020.587012 (2020).

53. Button, B. et al. A periciliary brush promotes the lung health by separating the mucus layer from airway epithelia. *Science* **337**, 937–41; 10.1126/science.1223012 (2012).

54. de Steenhuijsen Piters, W.A.A., et al. Interaction between the nasal microbiota and S. pneumoniae in the context of live-attenuated influenza vaccine. *Nat. Commun.* **10**, 2981; 10.1038/s41467-019-10814-9 (2019).

55. Liu, X., Wetzler, L.M., Nascimento, L.O. & Massari, P. Human airway epithelial cell responses to Neisseria lactamica and purified porin via Toll-like receptor 2-dependent signaling. *Infect Immun.* **78**, 5314–23; 10.1128/IAI.00681-10 (2010).

56. de Fays, C., Carlier, F.M., Gohy, S. & Pilette, C. Secretory immunoglobulin A immunity in chronic obstructive respiratory diseases. *Cells* **11**, 1324; 10.3390/cells11081324 (2022).

57. Firacative, C. et al. Identification of T helper (Th)1- and Th2-associated antigens of Cryptococcus neoformans in a murine model of pulmonary infection. *Sci. Rep.* **8**, 2681; 10.1038/s41598-018-21039-z (2018).

58. Khoury, D.S. et al. Measuring immunity to SARS-CoV-2 infection: comparing assays and animal models. *Nat. Rev. Immunol.* **20**, 727–38; 10.1038/s41577-020-00471-1 (2020).

59. Liu, C., Jiang, X., Gan, Y. & Yu, M. Engineering nanoparticles to overcome the mucus barrier for drug delivery: design, evaluation and state-of-the-art. *Med. Drug Discov.* **12**, 100110; 10.1016/j.medidd.2021.100110 (2021).

60. Honary, S. & Zahir, F. Effect of zeta potential on the properties of nano-drug delivery systems - A review (Part 1). *Trop. J. Pharm. Res.* **12**, 255–64; 10.1016/j.ijpharm.2024.124799 (2013).

61. Foroozandeh, P. & Aziz, A.A. Insight into cellular uptake and intracellular trafficking of nanoparticles. *Nanoscale Res. Lett.* **13**, 339; 10.1186/s11671-018-2728-6 (2018).

62. Newby, J.M. et al. Technologies strategies to estimate and control diffuse passage times through the mucus barrier in mucosal drug delivery. *Adv. Drug Deliv. Rev.* **124**, 64–81; 10.1016/j.addr.2017.12.002 (2018).

63. Li, M. et al. Enhanced intranasal delivery of mRNA vaccine by overcoming the nasal epithelial barrier via intra- and paracellular pathways. *J. Control. Release* **228**, 9–19; 10.1016/j.jconrel.2016.02.043 (2016).

64. Li, L. et al. Biodistribution, excretion, and toxicity of mesoporous silica nanoparticles after oral administration depend on their shape. *Nanomedicine* **11**, 1915–24; 10.1016/j.nano.2015.07.004 (2015).

65. He, X.X. et al. In vivo study of biodistribution and urinary excretion of surface-modified silica nanoparticles. *Analy. Chem.* **80**, 9597–603; 10.1021/ac801882g (2008).

66. Choi, H.S. et al. Renal clearance of nanoparticles. *Nat. Biotechnol.* **25**, 1165–70; 10.1038/nbt1340 (2009).

67. Arick, D.Q., Choi, Y.H., Kim, H.C. & Won, Y.-Y. Effects of nanoparticles on the mechanical functioning of the lung. *Adv. Colloid Interface Sci.* **225**, 218–28; 10.1016/j.cis.2015.10.002 (2015).

68. Gu, X. et al. Clearance of two organic nanoparticles from the brain via the paravascular pathway. *J. Control. Rel*. **322**, 31–41; 10.1016/j.jconrel.2020.03.009 (2020).

69. Formica, M.L. et al. On a highway to the brain: A review on nose-to-brain drug delivery using nanoparticles. *Appl. Mater. Today* **29**, 101631; 10.1016/j.apmt.2022.101631 (2022).

70. Hajdu, I. et al. Radiochemical synthesis and preclinical evaluation of 68Ga-labeled NODAGA-hydroxypropyl-beta-cyclodextrin (68Ga-NODAGA-HPBCD). *Eur. J. Pharm. Sci.* **128**, 202–8; 10.1016/j.ejps.2018.12.001 (2019).

71. Carter, N.J. & Curran, M.P. Live attenuated influenza vaccine (Flumist; Fluenz): a review of its use in prevention of seasonal influenza in children and adults. *Drugs* **71**, 1591–622; 10.2165/11206860-000000000-00000 (2011).

72. Mutsch, M. et al. Use of the inactivated intranasal influenza vaccine and the risk of Bell's palsy in Switzerland. N. Engl. J. Med. **350**, 896–903; 10.1056/NEJMoa030595 (2004).

73. Madhavan, M. et al. Tolerability and immunogenicity of an intranasally-administered adenovirus-vectored COVID-19 vaccine: An open-label partially-randomised ascending dose phase I trial. *EBioMedicine* **85**, 104298; 10.1016/j.ebiom.2022.104298 (2022).

74. Knudsen, K.B. et al. *In vivo* toxicity of cationic micelles and liposomes. *Nanomedicine* **11**, 467–77; 10.1016/j.nano.2014.08.004 (2015).

75. Zhang, P. et al. Nanoparticle size influences antigen retention and presentation in lymph node. *ACS Nano* **9**, 8480–93; 10.1021/acs.nanolett.9b02834 (2015).

76. Southam, D.S., Dolovich, M., O'Byrne, P.M. & Inman, M.D. Distribution of intranasal instillations in mice: effects of volume, time, body position, and anesthesia. *Am. J. Physiol. Lung Cell Mol. Physiol.* **282**, L833-9; 10.1152/ajplung.00173.2001 (2002).

77. Mitchell, M.J. et al. Engineering precision nanoparticles for drug delivery. *Nat. Rev. Drug Discov.* **20**, 101–24; 10.1038/s41573-020-0090-8 (2021).

78. Corthésy, B. Role of secretory IgA in infection and immunity. *Mucosal Immunol.* **6**, 535–42; 10.1016/j.autrev.2012.10.012 (2013).

79. Wright, P.F. et al. Longitudinal systemic and mucosal immune response to SARS-CoV-2 infection. *J. Infect. Dis.* **226**, 1204–14; 10.1093/infdis/jiac065 (2022).

80. Hartwell, B.L. et al. Intranasal vaccination with lipid-conjugated immunogens promotes antigen transmucosal uptake to drive mucosal and systemic immunity. *Sci. Transl. Med.* **14**, eabn1413; 10.1126/scitranslmed.abn1413 (2022).

81. Adhikari, K. & Verma, S.C. Neutralization antibody responses to SARS-CoV-2 variants after COVID-19 vaccination and boosters. *Vaccine* **24**, 100664; 10.1016/j.jvacx.2025.100664 (2025).

82. Bladh, O. et al. Comparison of SARS-CoV-2 spike-specific IgA and IgG in nasal secretions, saliva and serum. *Front. Immunol.* **15**, 1346749; 10.3389/fimmu.2024.1346749 (2024).

83. Riepler, L. et al. Comparison of four SARS-CoV-2 neutralization assays. *Vaccines* **9**, 13; 10.3390/vaccines9010013 (2020).

84. Klein, S.L. & Flanagan, K.L. Sex differences in immune responses. *Nat. Rev. Immunol.* **16**, 626–38; 10.1038/nri.2016.90 (2016).

85. Huang, L.-Y., Stuart, C., Takeda, K., D'Agnillo, F. & Golding, B. Poly(I:C) induces human lung endothelial barrier dysfunction by disrupting tight junction expression of claudin-5. *PloS One* **11**, e0160875; 10.1371/journal.pone.0160875 (2016).

86. Starkhammar, M. et al. Intranasal administration of poly(I:C) and LPS in BALB/c mice induces airway hyperresponsiveness and inflammation via different pathways. *PLoS One* **7**, e32110; 10.1371/journal.pone.0032110 (2012).

87. Misra, S.K., Kapoor, A. & Pathak, K. Nanovaccines for mucosal immunity (ed. Chavda, V.P. & Apostolopoulos, V.) 367–404 (Wiley online library) 10.1002/9781394175482.ch11 (2024).

88. WHO. Recommendations to assure the quality, safety and efficacy of influenza vaccines (human, live attenuated) for intranasal administration, Annex 4, *WHO Technical Report Series* No. 977
https://www.who.int/publications/m/item/influenza-attenuated-intranasal-administration-annex-4-trs-no-977 (2013).

89. Nair, A.B. & Jacob, S. A simple practice guide for dose conversion between animals and humans. *J. Basic Clin. Pharm.* **7**, 27–31; 10.4103/0976-0105.177703 (2016).

90. Đorđević, S. et al. Current hurdles to the translation of nanomedicines from bench to the clinic. *Drug Deliv. Transl. Res.* **12**, 500–25; 10.1007/s13346-021-01024-2 (2022).

91. Stöber, W., Fink, A. & Bohn, E. Controlled growth of monodisperse silica spheres in the micron size range. *J. Colloid Interface Sci.* **26**, 62–9; 10.1016/0021-9797(68)90272-5 (1968).

92. Severe Acute Respiratory Syndrome Coronavirus 2 Isolate Wuhan-Hu-1, co-Nucleotide-NCBI
https: //www.ncbi.nlm.nih.gov/nuccore/MN908947 (2020).

93. Dai, L. et al. Universal design of Betacoronavirus vaccines against COVID-19, MERS, and SARS. *Cell* **182**, 722–33; 10.1016/j.cell.2020.06.035 (2020).

94. Stadlbauer, D. et al. SARS-CoV-2 seroconversion in humans: A detailed protocol for a serological assay, antigen production, and test setup. *Curr. Protoc. Microbiol.* **57**, e100; 10.1002/cpmc.100 (2020).

95. Araújo, D.B. et al. SARS-CoV-2 isolation from the first reported patients in Brazil and establishment of a coordinated task network. *Mem. Inst. Oswaldo Cruz* **115**, e200342; 10.1590/0074-02760200342 (2020).

96. World Health Organization (WHO). Laboratory biosafety guidance related to the novel coronavirus (2019-nCoV). [Internet]. Geneve: WHO
https://www.who.int/docs/default-source/coronaviruse/laboratory-biosafety-novelcoronavirus-version-1-1.pdf?sfvrsn=912a9847_2 (2020).

97. Whittaker, A.L., Liu, Y. & Barker, T.H. Methods used and application of the mouse Grimace Scale in biomedical research 10 years on: a scoping review. *Animals* (Basel) **11**, 673; 10.3390/ani11030673 (2021).

98. Schmidt, F. et al. Measuring SARS-CoV-2 neutralizing antibody activity using pseudotyped and chimeric viruses. *J. Exp. Med.* **217**, e20201181; 10.1084/jem.20201181 (2020).

99. Quiros, P.M., Goyal, A., Jha, P. & Auwerx, J. Analysis of mtDNA/nDNA ratio in mice. *Curr. Protoc. Mouse Biol.* **7**, 47–54; 10.1002/cpmo.21 (2017).

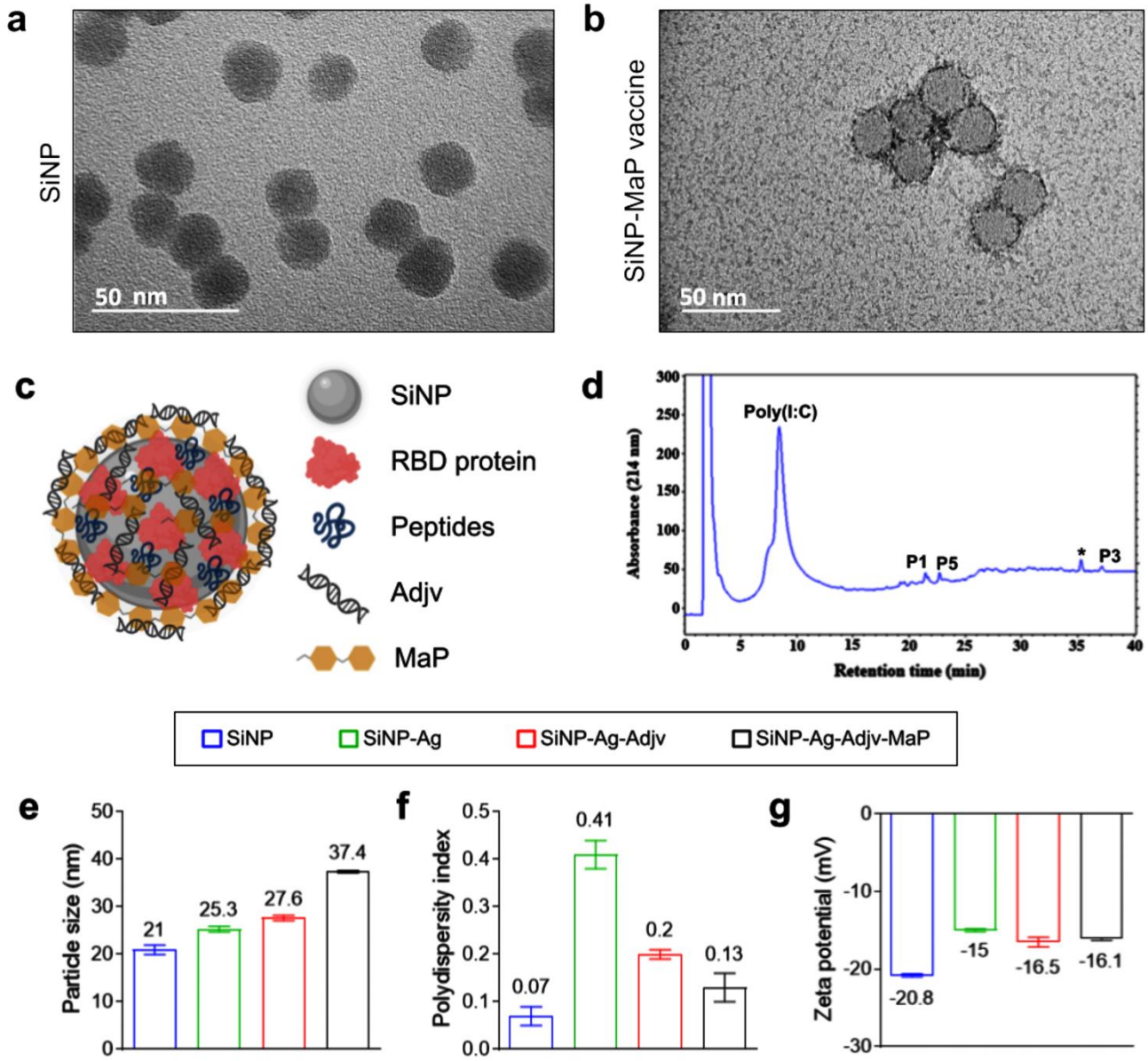

Figure 1. Characterization of SARS-CoV-2 nanoparticulate formulations. Transmission electron microscopy images of (**a**) silica mucus-penetrating nanoparticles (SiNP) and (**b**) these systems loaded with active components and functionalized with a mucoadhesive polymer (SiNP-MaP vaccine). (**c**) Schematic representation of the SiNP-MaP vaccine created in BioRender. Liberato, R. (2025) https://BioRender.com/e1pgkmq. (**d**) Chromatographic profile of the supernatant from the SiNP-Ag-Adjv nanoformulation at 214 nm, and * represents a contaminant present in the solvent system. The representative (**e**) particle size, (**f**) polydispersity index, and (**g**) zeta potential, as determined by dynamic light scattering (DLS), of mucus-penetrating empty silica-based nanoparticles (SiNP), antigens loaded into SiNP (SiNP-Ag), adjuvant incorporated into SiNP-Ag (SiNP-Ag-Adjv), and SiNP-Ag-Adjv functionalized with a mucoadhesive polymer (SiNP-Ag-Adjv-MaP). Data are presented as mean ± SD. Adjv – adjuvant; Ag –

RBD antigen; SiNP – silica-based nanoparticle; MaP – mucoadhesive polymer.

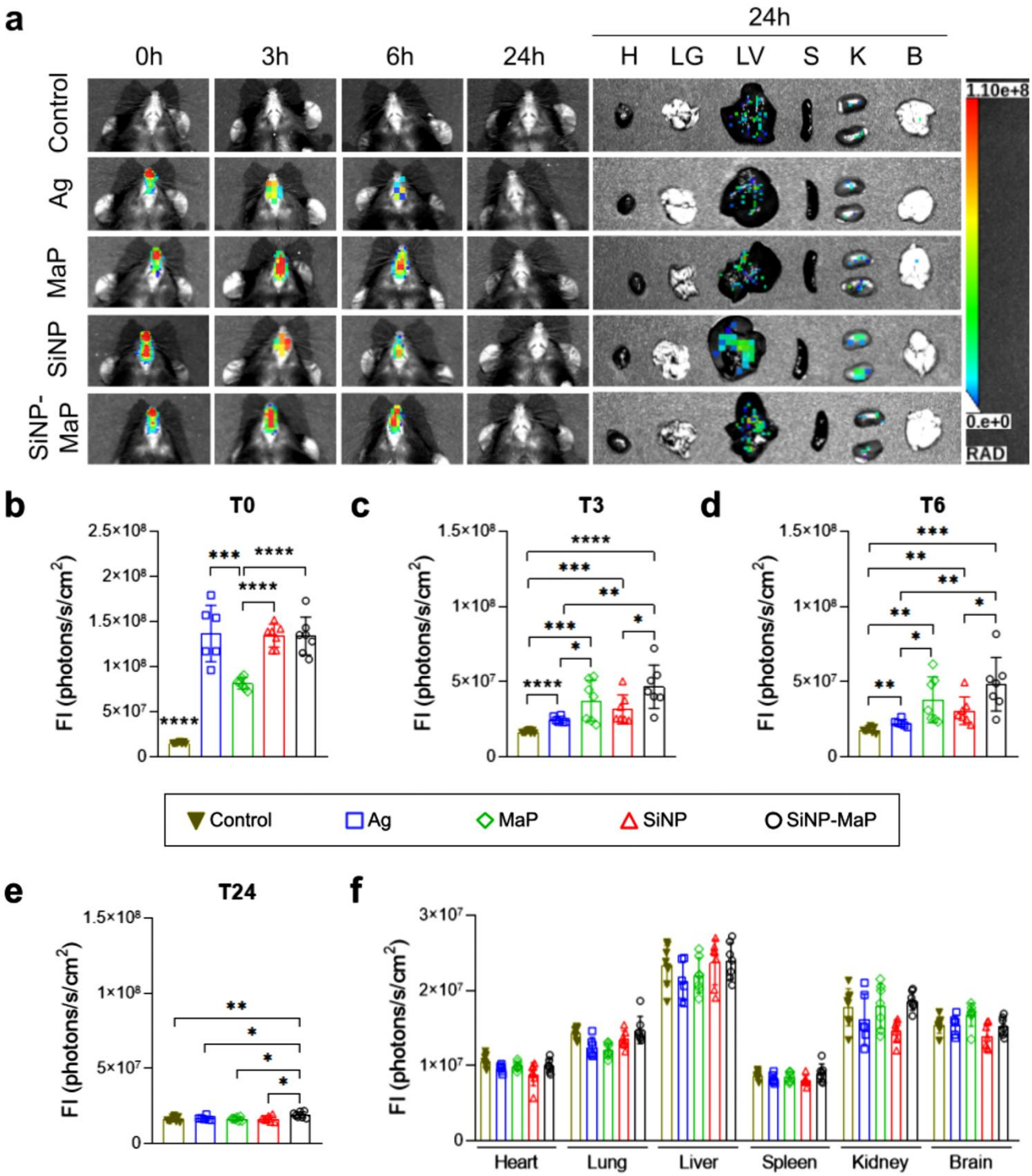

Figure 2. Nanovaccine residence time in the nasal cavity and antigen biodistribution. (**a**) In vivo fluorescence images of RBD biodistribution, comparing mice (n = 7-8/group) nasally instilled (10 µL) with a dose of 1) antigen alone (Ag, 20 µg/dose),

2) mucoadhesive polymer-coated Ag (MaP), 3) silica nanoparticle-carried Ag (SiNP), and 4) Ag loaded onto SiNP and functionalized by MaP (SiNP-MaP), along with control animals (non-immunized). The corresponding fluorescence intensity (FI) was measured in the animals at (**b**) 0 (T0), (**c**) 3 (T3), (**d**) 6 (T6), and (**e**) 24 hours (T24) post-instillation, and (**f**) in the different organs, including heart (H), lung (LG), liver (LV), spleen (S), kidney (K), and brain (B), at 24 hours post-nasal instillation. Data in (**b-f**) were represented as mean values ± SD and represent results from a single experiment. Differences between tested groups per time point or per organ were assessed using ANOVA followed by Tukey's multiple comparison test (three or more groups) or Student's *t*-test (two groups). $P < 0.05$ was considered statistically significant. *P < 0.05, **P < 0.01, ***P < 0.001, and ****P < 0.0001. The * without an indicator means the group's difference in relation to all others. Ag – RBD antigen; SiNP – silica-based nanoparticle; MaP – mucoadhesive polymer; s – second.

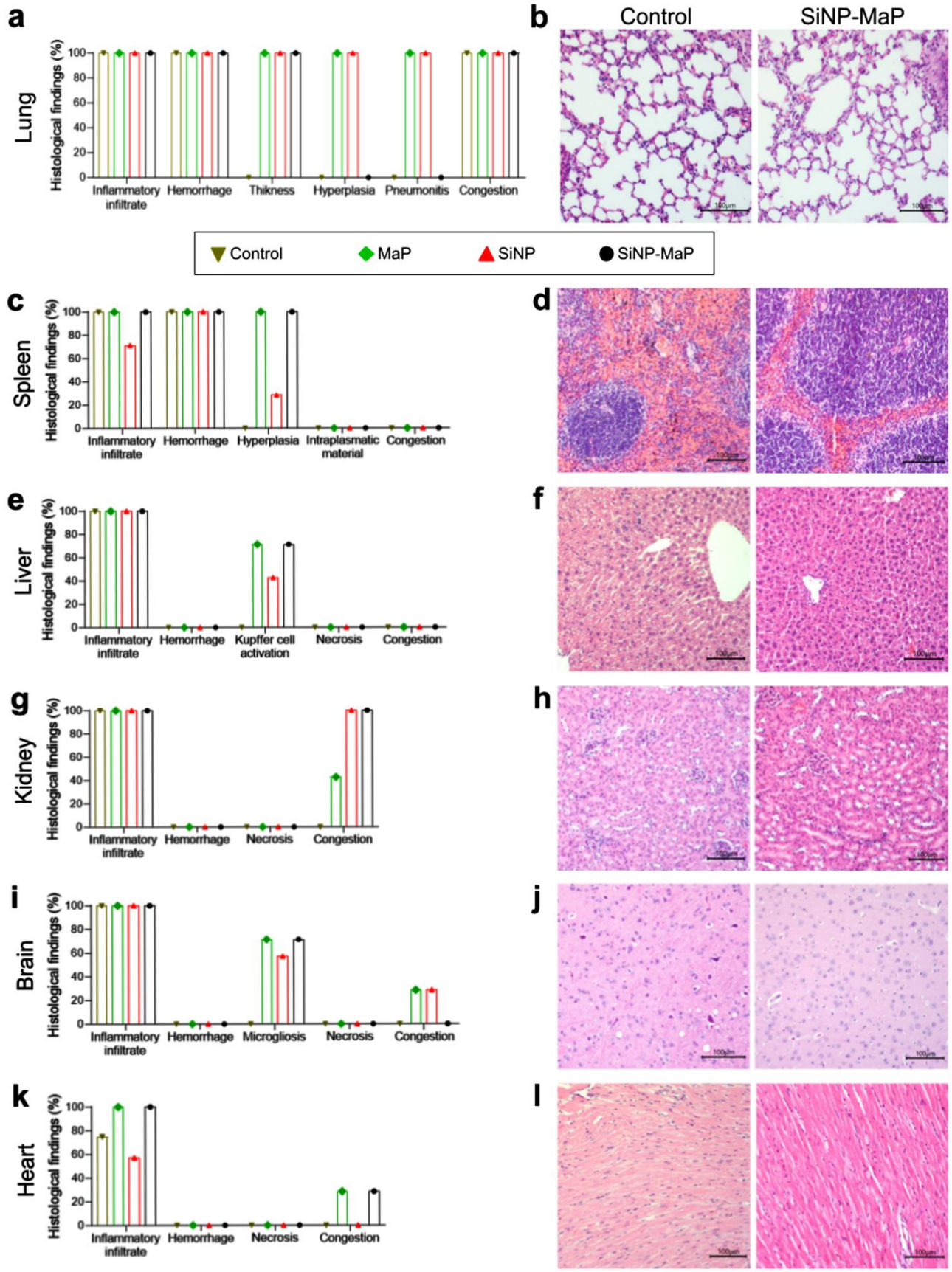
a
Lung
Histological findings (%)
Inflammatory infiltrate
Hemorrhage
Thikness
Hyperplasia
Pneumonitis
Congestion
b
Control
SiNP-MaP
Control
MaP
SiNP
SiNP-MaP
c
Spleen
Inflammatory infiltrate
Hemorrhage
Hyperplasia
Intraplasmatic material
Congestion
d
e
Liver
Inflammatory infiltrate
Hemorrhage
Kupffer cell activation
Necrosis
Congestion
f
g
Kidney
Inflammatory infiltrate
Hemorrhage
Necrosis
Congestion
h
i
Brain
Inflammatory infiltrate
Hemorrhage
Microgliosis
Necrosis
Congestion
j
k
Heart
Inflammatory infiltrate
Hemorrhage
Necrosis
Congestion
l

Figure 3. Histopathological analysis of target organs following intranasal instillation of the innovative mucoadhesive–mucopenetrating nanoparticulate system. One day after intranasal instillation (10 µL/dose) of (1) MaP vaccine, (2) SiNP vaccine, or (3) SiNP-MaP vaccine (n = 7/group), along with unimmunized control mice (n = 8), histopathological analyses were performed on different organs: (**a,b**) lung, (**c,d**) spleen, (**e,f**) liver, (**g,h**) kidney, (**i,j**) brain, and (**k,l**) heart. Panels (**a,c,e,g,i,k**) show the histopathological findings, while (**b,d,f,h,j,l**) display representative histopathological images highlighting the mild alterations observed in the control and SiNP-MaP groups, as the individual SiNP and MaP formulations exhibited similar histological features. Data in (**a,c,e,g,i,k**) are presented as mean values and represent results from a single experiment. Scale bar = 100 µm. SiNP – silica-based nanoparticle; MaP – mucoadhesive polymer.

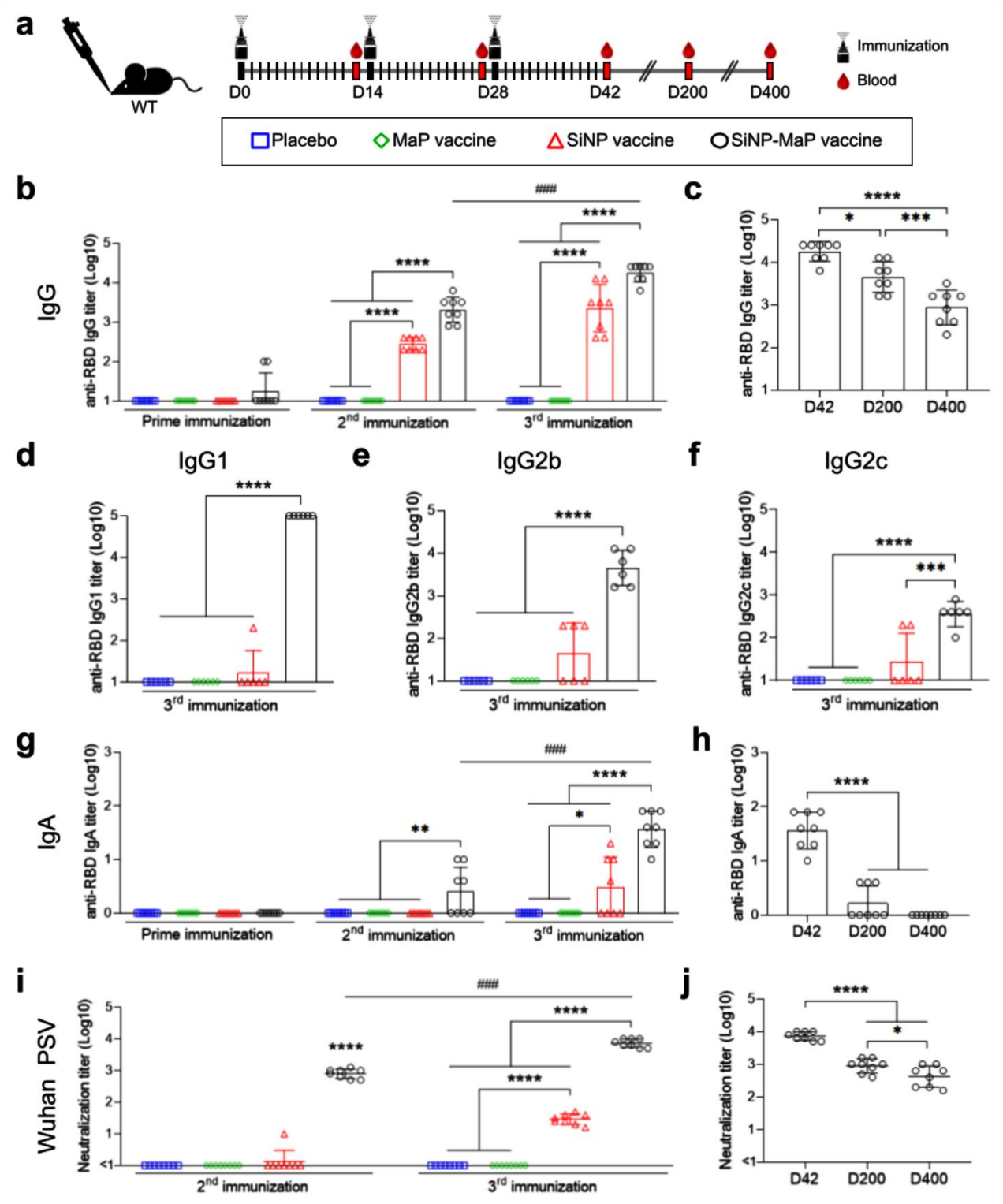

Figure 4. Systemic humoral immune responses after intranasal vaccination. (**a**) Wild-type (WT) mice (n = 8/group) were intranasally immunized with three doses (D0, D14, and D28, 10 μL/dose) of RBD protein (20 μg/dose) and peptides (5 μg/dose) plus

poly(I:C) adjuvant (20 μg/dose) without a nanoparticulate delivery system (Ag-Adjv), or functionalized with mucoadhesive polymer (MaP vaccine), or carried on mucus-penetrating silica-based nanoparticles (SiNP vaccine), or even the combination of these two delivery strategies (SiNP-MaP vaccine). Blood was collected and subjected to antibody response analysis (**b,d,e,g,i**) one day before and 14 days after the 3rd immunization, as well as (**c,f,h,j**) 6 months and 1 year after the 3rd dose with the SiNP-MaP vaccine. (**b,c**) RBD-specific IgG titer, (**d-f**) RBD-specific IgG isotypes, including IgG1, IgG2b, and IgG2c, and (**g,h**) RBD-specific IgA titer were determined by ELISA. Also, (**i,j**) neutralization of 50% inhibitory concentration (IC50) values was determined against wild-type SARS-CoV-2 pseudovirus (PSV) infection of 293T-hACE2 cells. Data representative of two independent experiments. Differences in antibody levels between animal groups per dose were assessed using one-way ANOVA followed by Tukey's multiple comparisons test (three or more groups) or Student's t-test (two groups). Data are expressed as mean ± SD. $P < 0.05$ was considered statistically significant. *$P < 0.05$, **$P < 0.01$, ***$P < 0.001$, and ****$P < 0.0001$. $^{\#}$ represents the difference between the second and third immunizations, $^{\#\#\#}P < 0.001$. D0 – day zero; D14 – day 14; D28 – day 28; D42 – day 42; D200 – day 200; D400 – day 400. WT – wild type; Ag – antigens; Adjv – adjuvant; SiNP – silica-based nanoparticle; MaP – mucoadhesive polymer.

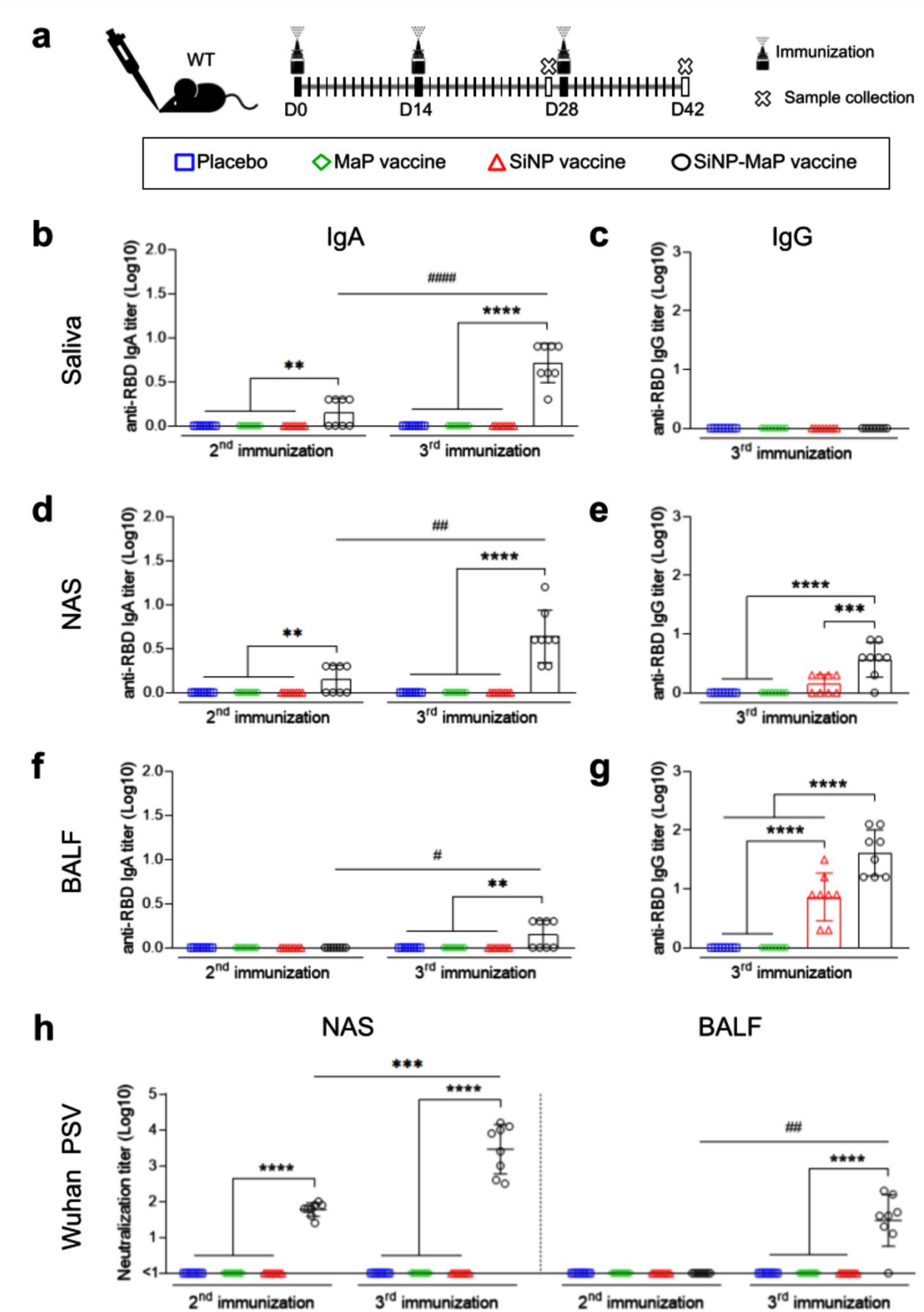
a
WT
D0
D14
D28
D42
Immunization
Sample collection
Placebo
MaP vaccine
SiNP vaccine
SiNP-MaP vaccine
b
IgA
c
IgG
Saliva
anti-RBD IgA titer (Log10)
anti-RBD IgG titer (Log10)
2nd immunization
3rd immunization
d
e
NAS
f
g
BALF
h
Wuhan PSV
Neutralization titer (Log10)

Figure 5. Mucosal humoral immune responses after intranasal immunization. (**a**) C57BL/6 female mice were immunized with two doses (D14, n = 8) or three doses (D28, n = 8) (10 µL/dose) of RBD protein (20 µL/dose) and peptides (5 µg/dose) plus poly(I:C) adjuvant (20 µg/dose) without a nanoparticulate system (Ag-Adjv), or coated with a mucoadhesive polymer (MaP vaccine), or carried on mucus-penetrating nanoparticles (SiNP vaccine), or even the combination of two delivery strategies (SiNP-MaP vaccine). Animals were anesthetized, and mucosal samples were collected on days 28 and 42. RBD-specific (**b,d,f**) IgA titers and (**c,e,g**) IgG titers were determined by ELISA in (**b,c**) saliva, (**d,e**) nasal-associated secretion (NAS), and (**f,g**) bronchoalveolar lavage fluid (BALF). Also, (**h**) neutralization of 50% inhibitory concentration (IC50) values was determined against wild-type SARS-CoV-2 pseudovirus (PSV) infection of 293T-hACE2 cells in NAS and BALF samples. Data representative of two independent experiments. Differences in antibody levels between animal groups per dose were assessed using one-way ANOVA followed by Tukey's multiple comparisons test (three or more groups) or Student's t-test (two groups). Data are expressed as mean ± SD. $P < 0.05$ was considered statistically significant. **$P < 0.01$, ***$P < 0.001$, and ****$P < 0.0001$. $^{\#}$ represents the difference between second and third immunization, $^{\#}P < 0.05$, $^{\#\#}P < 0.01$, and $^{\#\#\#\#}P < 0.0001$. D0 – day zero; D14 – day 14; D28 – day 28; D42 – day 42; WT – wild type; Ag – antigens; Adjv – adjuvant; SiNP – silica-based nanoparticle; MaP – mucoadhesive polymer.

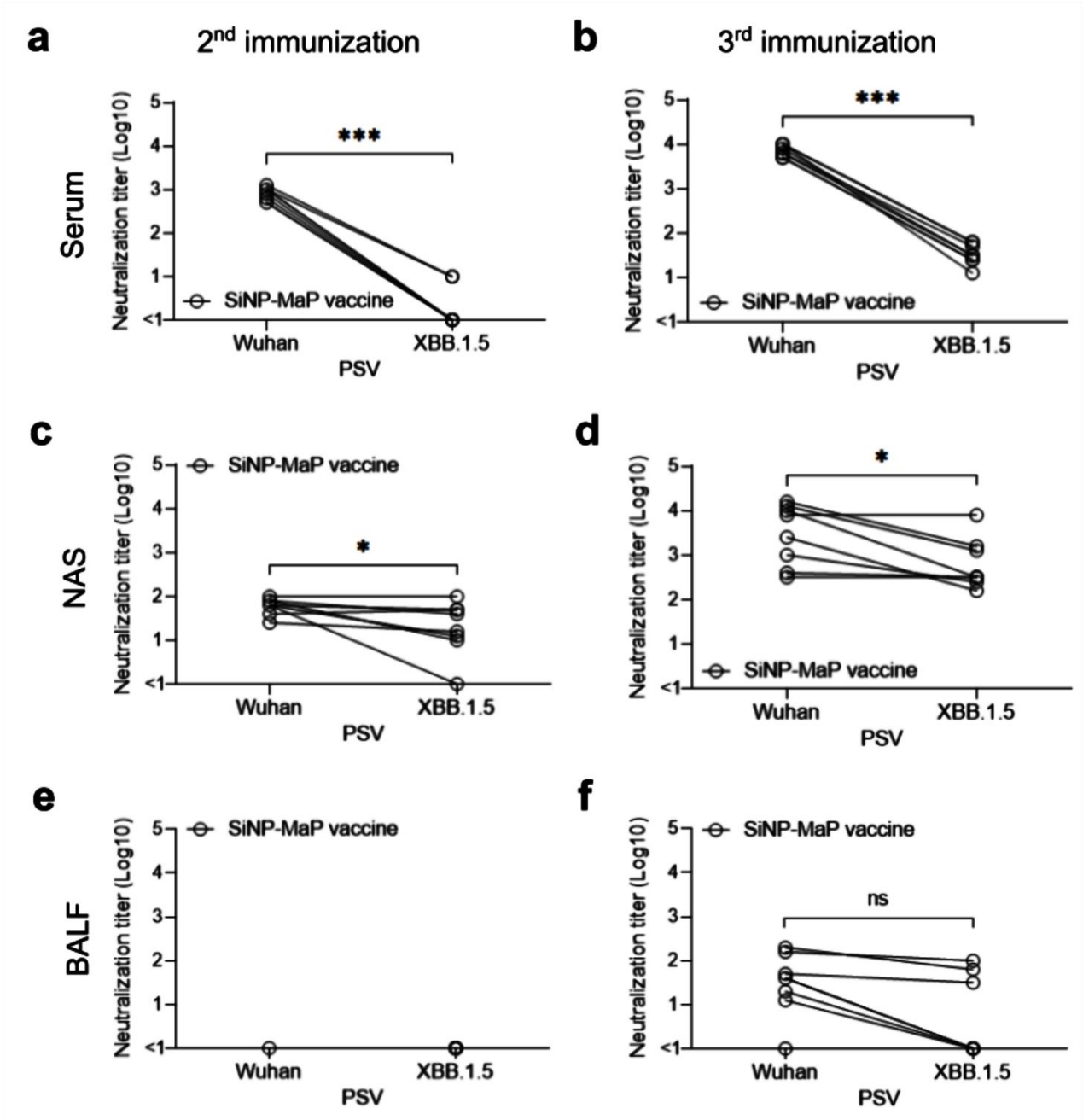

Figure 6. Variant-specific neutralizing antibody responses induced by intranasal SiNP-MaP vaccination. Neutralizing titers against SARS-CoV-2 pseudoviruses were measured in (**a,b**) serum, (**c,d**) nasal secretions (NAS), and (**e,f**) bronchoalveolar lavage fluid (BALF) from animals immunized with the SiNP-MaP vaccine collected after the (**a,c,e**) second and (**b,d,f**) third intranasal doses as depicted in Figures 4a and 5a. Samples were pre-incubated with pseudoviruses expressing the Wuhan or Omicron XBB.1.5 S protein and transferred to ACE2-expressing HT1080 cells. The half-maximal inhibitory concentration (IC50) was defined as the reciprocal dilution yielding a 50%

reduction in relative light units (RLU) versus virus control wells. Statistical analysis was performed using the Wilcoxon test for paired samples. Data are expressed as mean ± SD. P < 0.05 was considered statistically significant. *P < 0.05, ***P < 0.001, and ns – non significant. SiNP – silica-based nanoparticle; MaP – mucoadhesive polymer.

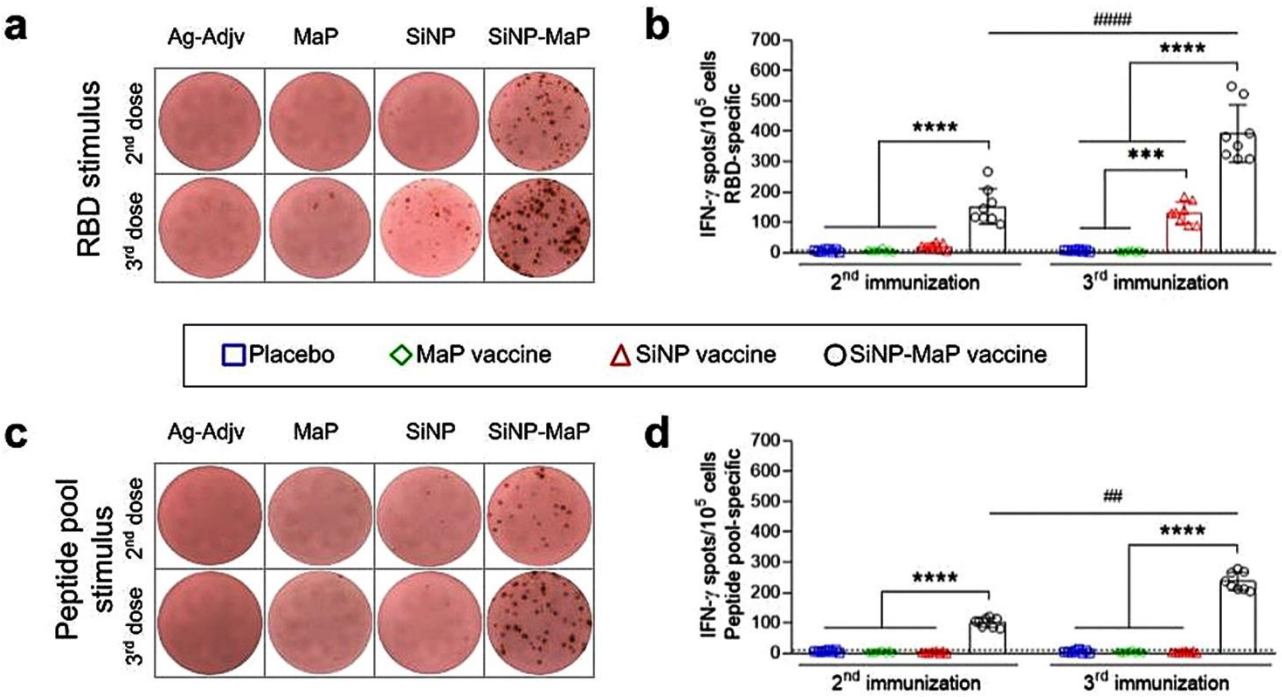

Figure 7. Cellular immune responses after intranasal immunization. Animals were immunized as depicted in Figure 4a (n = 8) with the same formulations previously tested. RBD protein and peptides plus poly(I:C) adjuvant without a nanoparticulate system (Ag-Adjv), or coated with a mucoadhesive polymer (MaP), or carried on mucus-penetrating nanoparticles (SiNP), or even the combination of two delivery strategies (SiNP-MaP). Animal spleens were collected, and splenocytes were isolated on days 28 and 42. IFN-γ-producing splenocytes (per 3 x 10^5 cells) induced by stimulation with 10 µg/mL of (**a,b**) protein RBD and (**c,d**) peptide pool were detected by ELISPOT. (**a,c**) Images displaying representative results near the average value are presented in the left panels. The dotted line indicates the lower limit of detection (7.23 and 8.27 SFU/10^5 cells for RBD and peptide pool stimuli, respectively). Data representative of two independent experiments. Differences in antibody levels between animal groups per dose were assessed using one-way ANOVA followed by Tukey's multiple comparisons test (three or more groups) or Student's t-test (two groups), where **P < 0.01 and ****P < 0.0001. # represents the difference between second and third immunization, ##P < 0.01, and ####P < 0.0001. Data are expressed as mean ± SD. Ag – antigens; Adjv – adjuvant; SiNP – silica-based nanoparticle; MaP – mucoadhesive polymer.

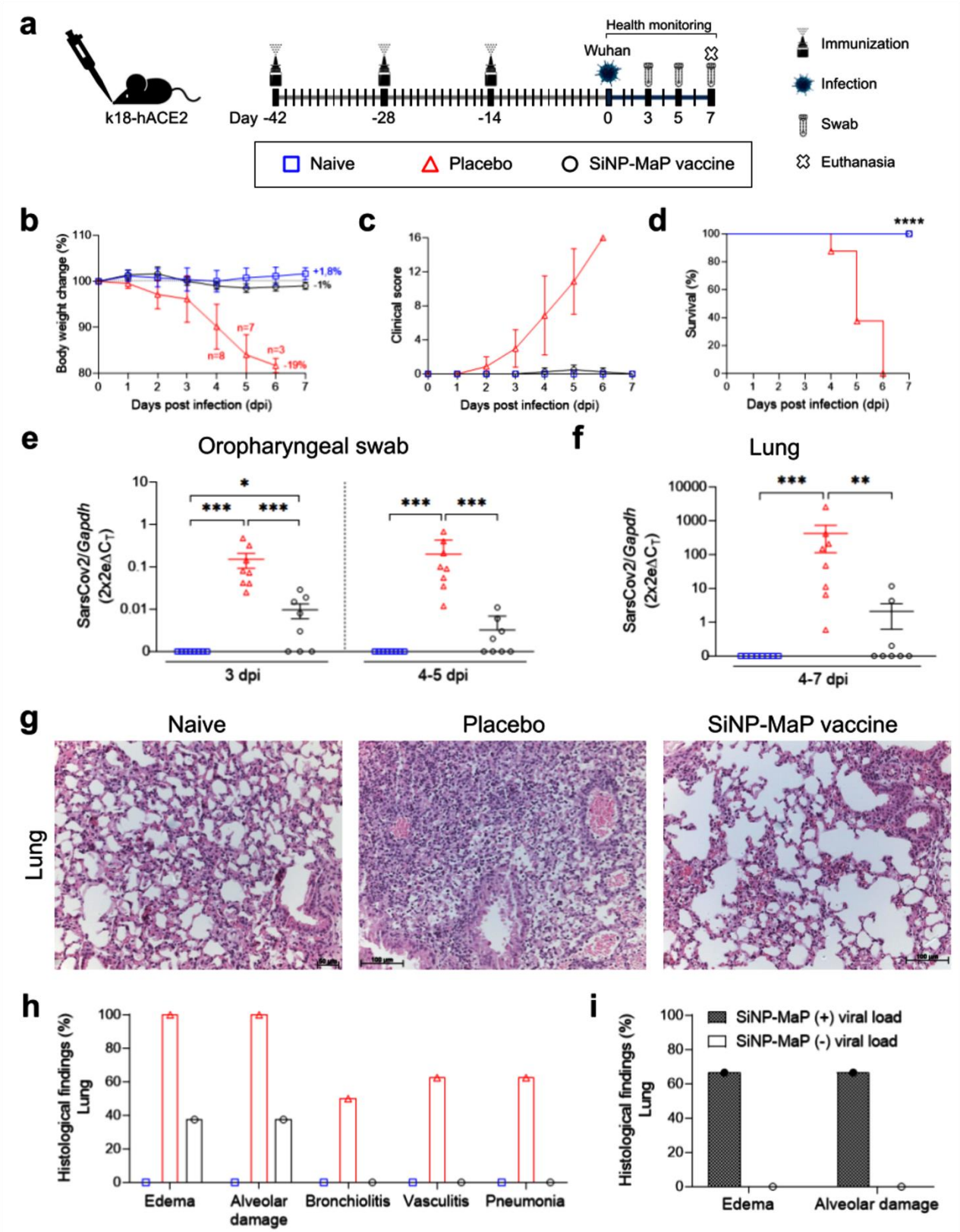
a
k18-hACE2
Day -42
-28
-14
0
3
5
7
Health monitoring
Wuhan
Immunization
Infection
Swab
Euthanasia
Naive
Placebo
SiNP-MaP vaccine
b
Body weight change (%)
Days post infection (dpi)
+1.8%
-1%
-19%
n=7
n=3
n=8
c
Clinical score
Days post infection (dpi)
d
Survival (%)
Days post infection (dpi)
****
e
Oropharyngeal swab
SarsCov2/Gapdh (2x2e-ΔCT)
3 dpi
4-5 dpi
f
Lung
SarsCov2/Gapdh (2x2e-ΔCT)
4-7 dpi
g
Naive
Placebo
SiNP-MaP vaccine
Lung
h
Histological findings (%) Lung
Edema
Alveolar damage
Bronchiolitis
Vasculitis
Pneumonia
i
SiNP-MaP (+) viral load
SiNP-MaP (-) viral load
Histological findings (%) Lung
Edema
Alveolar damage

Figure 8. Protective efficacy of SARS-CoV-2 intranasal SiNP-MaP nanovaccine against wild-type SARS-CoV-2 infection in hACE2-transduced mice. (**a**) The SiNP-MaP vaccine was administered intranasally in a 3-dose regimen (D-42, D-28, and D-14, 10 µL/dose) to K18-hACE2 transgenic mice (n = 8/group). For comparison, a naïve group (non-immunized and non-infected) and a placebo group (immunized with SiNP-MaP without antigens and infected) were included. Animals were intranasally challenged with 1 x 10^5 PFU (lethal dose, 10 µL/dose) of live wild-type SARS-CoV-2 on day 0, and health monitoring was observed for 7 days post-infection, at which point the surviving animals were euthanized and the lungs collected. Oropharyngeal swabs (days 3, 5, and 7 post-infection) were collected. Changes in (**b**) body weight, (**c**) clinical score, and (**d**) survival were observed from day 0 to 7. Viral load in oropharyngeal swabs on (**e**) 3 dpi and 5 dpi and (**f**) lungs was analyzed. (**g**) Pathological changes in the lungs of animals after challenge by histological analysis, and (**h,i**) frequency of histopathological findings at 4-7 dpi comparing (**h**) all tested groups and (**i**) viral load positive and negative SiNP-MaP animals. Data in (**b,c,e,f**) were represented as mean ± SD, and (**d,h,i**) as mean values. All data are representative results from a single experiment. Differences between the animal groups were assessed using Tukey's multiple comparisons test (three or more groups) or Student's t-test (two groups). Values of $P < 0.05$ were considered statistically significant. *$P < 0.05$, **$P < 0.01$, ***$P < 0.001$. D-42 – day minus 42; D-28 – day minus 28; D-14 – day minus 14; D-1 – day minus 1; D0 – day 0; D3 – day 3; D5 – day 5; D7 – day 7; WT – wild type; SiNP – silica-based nanoparticle; MaP – mucoadhesive polymer; dpi – days post-infection.